Computers and Mathematics with Applications 70 (2015) 1266–1289

Contents lists available at ScienceDirect

Computers and Mathematics with Applications

journal homepage: www.elsevier.com/locate/camwa

On the algorithmic and implementational aspects of a Discontinuous Galerkin method at finite strains

Timothy J. Truster [a,b,*,1], Pinlei Chen [b,2], Arif Masud [b,3]

[a] Department of Civil and Environmental Engineering, University of Tennessee, Knoxville, 318 John D. Tickle Engineering Building, Knoxville, TN 37921, United States

[b] Department of Civil and Environmental Engineering, University of Illinois at Urbana-Champaign, 3129E Newmark Civil Engineering Laboratory, MC-250, Urbana, IL 61801-2352, United States

ARTICLE INFO

Article history:
Received 16 July 2014
Received in revised form 20 March 2015
Accepted 29 June 2015
Available online 14 August 2015

Keywords:
Discontinuous Galerkin
Stabilization
Finite strain
Variational consistency
Adjoint consistency
Variational multiscale

ABSTRACT

In this work, algorithmic modifications are proposed and analyzed for a recently developed stabilized finite strain Discontinuous Galerkin (DG) method. The distinguishing feature of the original method, referred to as VMDG, is a consistently derived expression for the numerical flux and stability tensor that account for evolving material and geometric nonlinearity in the vicinity of the interface. Herein, the proposed modifications involve simplifications to the residual force vector and tangent stiffness matrix of the VMDG method that lead to formulations similar to other existing DG methods but retain the enhanced definition for the stability parameters. The primary objective is to reduce the costs associated with implementing the method as well as executing simulations while retaining accuracy and flexibility, thereby making the formulation amenable to boarder material classes such as inelasticity. Each simplification has associated implications on the mathematical and algorithmic properties of the method, such as L^2 convergence rate, solution accuracy, continuity enforcement, and stability of the nonlinear equation solver. These implications are carefully quantified and assessed through a comprehensive numerical performance study. The range of two and three dimensional problems under consideration involves both isotropic and anisotropic materials. Both triangular and quadrilateral element types are employed along with h and p refinement. The ability of the proposed methods to produce stable and accurate results for such a broad class of problems is highlighted.

1. Introduction

Recently, a stabilized Discontinuous Galerkin (DG) method was developed by Truster et al. [1] for modeling large strain solid mechanics problems. The method, denoted herein as the Variational Multiscale Discontinuous Galerkin (VMDG) method, is consistently derived from an underlying Lagrange multiplier interface formulation and possesses a form

* Corresponding author at: Department of Civil and Environmental Engineering, University of Tennessee, Knoxville, 318 John D. Tickle Engineering Building, Knoxville, TN 37921, United States. Tel.: +1 865 974 1913; fax: +1 865 974 2669.
E-mail address: ttruster@utk.edu (T.J. Truster).
1 Assistant Professor.
2 Graduate Research Assistant.
3 Professor of Mechanics and Structures.

http://dx.doi.org/10.1016/j.camwa.2015.06.035
0898-1221/

analogous to the symmetric interior penalty Galerkin method [2]. Its novel feature is that computable expressions emerge during the course of the derivation for the stability tensor and numerical flux weighting tensors that account for geometric and material nonlinearity. While accurate and stable results were obtained for problems involving large rotations and nonconforming interfaces, the formulation is more involved to implement than the classical DG method. Namely, its consistent linearization involves the nonstandard inclusion of the sixth-order tensor of material moduli, which is the derivative of the tangent material moduli. This higher order tensor can be difficult to derive in closed-form and subsequently implement for complicated material models, particularly materials exhibiting history dependence such as plasticity. Thus, while the VMDG method is mathematically and mechanically sound, the formulation would benefit from carefully designed modifications to reduce the complexity of implementation and cost of computation while maintaining superior mathematical properties, thereby increasing its appeal to the mechanics community.

Additionally, the existing literature on theoretical and computational aspects of DG methods for nonlinear solid mechanics possesses some gaps. The fundamental theory for DG methods applied to linear PDEs has become well-established; see e.g. the analyses and references from the treatise by Arnold et al. [2]. However, theorems and analyses conducted in the linear context do not always carry over to the nonlinear context. For example, many existing DG methods for finite strains, including those for hyperelasticity [3], plasticity [4], and second-order computational homogenization [5], possess a nonsymmetric incremental weak form. Loss of symmetry has been shown in the linear context [6] to upset adjoint consistency as well as yielding suboptimal L^2 error convergence rates. While studies on adjoint consistency have been performed for nonlinear fluid mechanics [7], the suboptimal L^2 convergence has not been demonstrated or investigated for DG methods for nonlinear solid mechanics. Fewer nonlinear DG methods employ symmetric tangent matrices; examples include [1,8]. Another noteworthy symmetric DG formulation was developed by Lew and co-workers [9], for which extensive stability and accuracy analyses were conducted in [10]. In contrast to the classical interior penalty approach, their formulation employs the concept of interface lifting operators, previously analyzed for linear PDEs in [2,11]. More recently, the hybridizable DG method [12,13] has emerged which utilizes numerical traces to treat the inter-element continuity constraints. The benefit of this alternative approach is that element interior fields consisting of the displacement and strain fields can be condensed locally to leave the trace field as the only global unknown field, yielding significant cost savings. Finite strain hybrid DG formulations are presented in [14,15], where the latter was shown to possess a variational structure. However, amongst all the preceding methods, the design of the stability parameter is crucial to obtaining stable computed response, particularly in the nonlinear context. The idea of adapting [10] or evolving [1] the stability parameter with solution nonlinearity has received little attention in the literature. In summary, the preceding developments for solid mechanics DG methods would be greatly enhanced by qualitatively investigating the effects of method attributes such as symmetry and stability parameter definition upon the method performance such as accuracy and number of required Newton–Raphson iterations.

The objective of this paper is to propose a family of algorithmic modifications to the VMDG method [1] and systematically analyze their mathematical and algorithmic properties. These modifications consist of selectively neglecting terms in the interface nonlinear and incremental weak forms, resulting in both symmetric and nonsymmetric formulations reminiscent of other existing methods [3,4,8]. Throughout, emphasis is placed on analyzing how these simplifications affect the balance of ease of implementation, computational efficiency, and numerical accuracy across a range of problems. Insights into this balance are gained through carefully designed numerical studies involving large strains and rotations, isotropic and anisotropic materials, and h and p refinement. Specific measures of performance include (i) maximum convergent load level, (ii) number of Newton–Raphson iterations, (iii) cost of element integration, (iv) convergence rate in L^2 and H^1 norms with respect to analytical solutions, and (v) accuracy compared to continuous Galerkin (CG) benchmarks. Additionally, we investigate the tensorial nature of the stability tensors in the VMDG method with respect to material and geometric nonlinearity. The results of these numerical investigations provide insight into the mathematical and algorithmic properties of the VMDG method and other existing nonlinear interior penalty DG methods as well as providing a reference point for methods employing lifting operators or hybridization. Finally, the proposed simplifications enable the ready extension of the VMDG method to wider classes of materials, including inelasticity, by removing the need to evaluate the sixth-order algorithmic material moduli and by minimizing the additional computational cost at integration points.

We begin in Section 2 with a brief review of the VMDG method [1] and highlight the major equations. Then, various simplifications are proposed in Section 3 and evaluated through a comparison of numerical results in Section 4. Conclusions concerning the algorithmic attributes are drawn in Section 5.

2. Review of a finite strain stabilized discontinuous Galerkin method: VMDG

Let $\Omega \subset \mathbb{R}^{n_{sd}}$ be a mechanical body that is acted upon by a deformation $\boldsymbol{\phi}$. We denote a point in the reference configuration as $\boldsymbol{X} \in \Omega$ and its image in the current configuration as $\boldsymbol{x} \in \Omega_\phi$. The deformation gradient associated with $\boldsymbol{\phi}$ is defined by $\boldsymbol{F} = \partial \boldsymbol{x}/\partial \boldsymbol{X}$. The classical weak form of the governing equilibrium equation is stated as: Find $\boldsymbol{\phi} \in \mathcal{S}$ such that for all variations $\boldsymbol{\eta}_o \in \mathcal{V}$:

$$\int_\Omega \text{GRAD}\, \boldsymbol{\eta}_o : \boldsymbol{P}\, \text{d}V = \int_\Omega \boldsymbol{\eta}_o \cdot \rho_o \boldsymbol{f}\, \text{d}V + \int_{\Gamma_\sigma} \boldsymbol{\eta}_o \cdot \boldsymbol{T}\, \text{d}A \tag{1}$$

in which the following notation is adopted: $\boldsymbol{N}$ is the unit outward normal on domain boundary $\partial\Omega$, $\boldsymbol{f}$ is the body force, $\boldsymbol{T}$ is the prescribed traction on $\Gamma_\sigma \subset \partial\Omega$, and $\boldsymbol{g}$ is the prescribed displacement on $\Gamma_u \subseteq \partial\Omega$. The portions of the boundary Γ_σ and Γ_u satisfy $\Gamma_\sigma \cap \Gamma_u = \varnothing$, $\Gamma_\sigma \cup \Gamma_u = \partial\Omega$. Also, $\mathcal{S}$ and $\mathcal{V}$ are appropriate spaces of trial and test functions satisfying the Dirichlet boundary conditions and appropriate smoothness properties [1]. Finally, $\boldsymbol{P}$ is the first Piola–Kirchhoff stress tensor. While the developments that follow accommodate general constitutive relations, we will focus on the case of hyperelasticity whereby $\boldsymbol{P}$ is related to the deformation gradient $\boldsymbol{F}$ through a strain–energy density function Ψ according to $\boldsymbol{P} = \partial\Psi/\partial\boldsymbol{F}$.

Herein, we consider discontinuous approximations of the solution field $\boldsymbol{\phi}$. Let $\mathcal{T}$ be a discretization of Ω into disjoint open regions Ω_e called elements such that $\bigcup_e \bar{\Omega}_e = \bar{\Omega}$. We denote the union of element interiors and boundaries as $\tilde{\Omega}$ and $\tilde{\Gamma}$, respectively. Three subsets of element boundaries are considered: traction-type $\tilde{\Gamma}_\sigma = \tilde{\Gamma} \cap \Gamma_\sigma$, displacement-type $\tilde{\Gamma}_u = \tilde{\Gamma} \cap \Gamma_u$, and interior-type $\tilde{\Gamma}_I = \tilde{\Gamma} \backslash \left(\tilde{\Gamma}_\sigma \cup \tilde{\Gamma}_u\right)$. The discrete solution space $\mathcal{S}^h$ is taken to be the space of polynomial functions of order k that are continuous on elements $\Omega_e \in \mathcal{T}$ but possibly discontinuous along element interfaces $\tilde{\Gamma}_I$. With these preceding conventions in hand, the stabilized discontinuous Galerkin formulation associated with (1) as proposed in [1] is expressed as:

$$R\left(\boldsymbol{\eta}_o^h; \boldsymbol{\phi}^h\right) = \underbrace{\int_{\tilde{\Omega}} \text{GRAD}\ \boldsymbol{\eta}_o^h : \boldsymbol{P}^h\ \text{d}V}_{R0} + \underbrace{\int_{\tilde{\Gamma}_I} \left[\!\left[\boldsymbol{\eta}_o^h\right]\!\right] : \left(\boldsymbol{\tau}_s \cdot \left[\!\left[\boldsymbol{\phi}^h\right]\!\right]\right)\ \text{d}A}_{R1} - \underbrace{\int_{\tilde{\Gamma}_I} \left[\!\left[\boldsymbol{\eta}_o^h\right]\!\right] : \left\{\boldsymbol{P}^h\right\}\ \text{d}A}_{R2}$$
$$- \underbrace{\int_{\tilde{\Gamma}_I} \left\{\text{GRAD}\ \boldsymbol{\eta}_o^h : \mathbf{A}^h\right\} : \left[\!\left[\boldsymbol{\phi}^h\right]\!\right]\ \text{d}A}_{R3} - \underbrace{\int_{\tilde{\Omega}} \boldsymbol{\eta}_o^h \cdot \rho_o \boldsymbol{f}\ \text{d}V}_{F\Omega} - \underbrace{\int_{\tilde{\Gamma}_\sigma} \boldsymbol{\eta}_o^h \cdot \boldsymbol{T}\ \text{d}A}_{F\Gamma} = 0 \tag{2}$$

in which $\mathbf{A}^h$ is the fourth-order acoustic tensor of material moduli $\mathbf{A}^h = \partial\boldsymbol{P}^h/\partial\boldsymbol{F}$. Also, the superscript h has been inserted to indicate the finite-dimensional counterparts of the continuum fields. As is typical amongst DG methods, we note that $\mathcal{S}^h \not\subset \mathcal{S}$ due to the use of discontinuous trial functions. In the sections that follow, we refer to the combination of (2) with its corresponding consistent linearization as the Variational Multiscale Discontinuous Galerkin (VMDG) method in reference to its derivation employing Variational Multiscale concepts [1,16,17].

For subsequent discussions, we have labeled each term within (2) in order to isolate its purpose within the weak form. The standard Galerkin term $R0$ enforces equilibrium on element interiors and follows directly from the first term in (1). The terms $F\Omega$ and $F\Gamma$ represent the external forces applied within the body and along the boundary Γ_σ, respectively, as appearing on the right-hand side of (1). The penalty term $R1$ plays the key role of stabilizing the present DG formulation, whereas in the classical penalty method it serves to weakly impose the inter-element continuity of $\boldsymbol{\phi}^h$. This role is instead fulfilled by $R3$, which we call the symmetrizing term. Finally, $R2$ serves to weakly enforce traction equilibrium along the $\tilde{\Gamma}_I$ and is designated as the average-stress term; this term ensures the variational consistency of the method. These roles are made readily apparent by examining an underlying Lagrange multiplier interface formulation, for which the reader is referred to [1].

Remark. The Dirichlet boundary conditions could also be weakly imposed in a similar manner as inter-element continuity through the addition of integrals along $\tilde{\Gamma}_u$. However, herein we have elected to strongly enforce $\boldsymbol{\phi}^h = \boldsymbol{g}$ within the definition of $\mathcal{S}^h$ both within the theoretical developments and the subsequent numerical studies in order to focus on the performance of the inter-element DG contributions.

The interface terms in (2) are a function of the so-called jump operator and averaging operator, which are defined as follows for an adjacent element pair $\Omega_e^{(+)}$ and $\Omega_e^{(-)}$:

$$\left[\!\left[\boldsymbol{\phi}^h\right]\!\right] = \boldsymbol{\phi}^{h(+)} \otimes \boldsymbol{N}^{(+)} + \boldsymbol{\phi}^{h(-)} \otimes \boldsymbol{N}^{(-)} \tag{3}$$
$$\left\{\boldsymbol{P}^h\right\} = \boldsymbol{\delta}_s^{(+)} \cdot \boldsymbol{P}^{h(+)} + \boldsymbol{\delta}_s^{(-)} \cdot \boldsymbol{P}^{h(-)} \tag{4}$$
$$\left\{\text{GRAD}\ \boldsymbol{\eta}_o^h : \mathbf{A}^h\right\} = \boldsymbol{\delta}_s^{(+)} \cdot \left(\text{GRAD}\ \boldsymbol{\eta}_o^{h(+)} : \mathbf{A}^{h(+)}\right) + \boldsymbol{\delta}_s^{(-)} \cdot \left(\text{GRAD}\ \boldsymbol{\eta}_o^{h(-)} : \mathbf{A}^{h(-)}\right) \tag{5}$$

where we have adopted element-numbering invariant definitions that are presented in [18].

As shown in [1,17], definitions for the weighting tensors $\boldsymbol{\delta}_s^{(\alpha)}$ in (4) arise naturally from modeling the effects of fine scales within Lagrange multiplier interface formulations:

$$\boldsymbol{\tau}_s = \left(\boldsymbol{\tau}_s^{(+)} + \boldsymbol{\tau}_s^{(-)}\right)^{-1}, \qquad \boldsymbol{\delta}_s^{(\alpha)} = \boldsymbol{\tau}_s \cdot \boldsymbol{\tau}_s^{(\alpha)} \tag{6}$$

where α takes the value $+/-$ to designate the quantity on the corresponding side of the elemental interface. The stability tensors $\boldsymbol{\tau}_s^{(\alpha)}$ are evaluated in terms of edge bubble functions modeling the fine scales within each element $\Omega_e^{(\alpha)}$:

$$\boldsymbol{\tau}_s^{(\alpha)} = b_{s,ave}^{(\alpha)} \tilde{\boldsymbol{\tau}}_s^{(\alpha)} = \left[\text{meas}\left(\gamma_s\right)\right]^{-1} \left(\int_{\gamma_s} b_s^{(\alpha)}\ \text{d}A\right)^2 \left[\int_{\omega_s^{(\alpha)}} \text{GRAD}\ \boldsymbol{b}_s^{(\alpha)} : \mathbf{A}^{h(\alpha)} : \text{GRAD}\ \boldsymbol{b}_s^{(\alpha)}\ \text{d}V\right]^{-1} \tag{7}$$

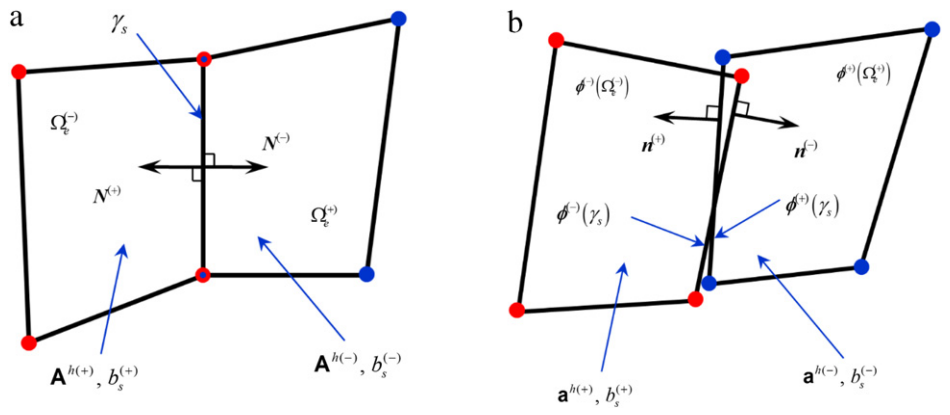

Fig. 1. Element pair $\Omega_e^{(+)}$ and $\Omega_e^{(-)}$ sharing interface segment γ_s: (a) reference configuration; (b) current configuration.

where γ_s denotes the common boundary segment between elements $\Omega_e^{(+)}$ and $\Omega_e^{(-)}$, and $\omega_s^{(\alpha)} \subseteq \Omega_e^{(\alpha)}$ is the sector of support for the bubble $\boldsymbol{b}_s^{(\alpha)} = \sum_{J=1}^{n_{\text{sd}}} b_s^{(\alpha)} \boldsymbol{E}_J$. Herein, we take the bubble functions $b_s^{(\alpha)}$ to be higher order polynomials ($m > k$) that vanish on the boundaries of the sector $\omega_s^{(\alpha)}$ not in contact with the segment γ_s. Further elaboration on these definitions is provided in [1,17].

We highlight three key features of the stabilization terms as derived in [1]:

1. When $\boldsymbol{\tau}_s^{(+)} \neq \boldsymbol{\tau}_s^{(-)}$, the tensors $\boldsymbol{\delta}_s^{(\alpha)}$ from (6) induce a weighted average definition of the numerical flux in (4)–(5). Through the explicit dependence on the sector $\omega_s^{(\alpha)} \subseteq \Omega_e^{(\alpha)}$, the edge bubble function $b_s^{(\alpha)}$, and the material tensor $\mathbf{A}^{h(\alpha)}$ according to (7), the weighting tensors account for (i) element size, (ii) element shape, (iii) polynomial order, (iv) and material properties. Improvements in the accuracy of computed results on cruder discretizations has been demonstrated by other authors [17,19].
2. The effects of geometric and material nonlinearity are incorporated through the dependence of $\mathbf{A}^{h(\alpha)}$ on the deformation $\boldsymbol{\phi}^{h(\alpha)}$. The evolution of the stability tensors derived from evolving $\boldsymbol{\phi}^{h(\alpha)}$ during quasi-static loading histories will be exhibited in the numerical results of Section 4. Previous studies [1,10] have demonstrated enhanced stability under large deformations by adapting the penalty parameter according to geometric and material nonlinearity.
3. The stability parameters contained in (6) and (7) are tensorial quantities, which is a unique feature of the present approach that arises from the derivations in [1,17].

An illustrative example of the preceding definitions is presented in Fig. 1 for the case of two quadrilateral elements; while the elements shown share an entire edge, generalizing the preceding definitions to partial element segments is easily accomplished [1,17]. Observe that while the element boundaries initially coincide along $\gamma_s \subset \tilde{\Gamma}_I$ in the reference configuration, the image of the boundaries in the deformed configuration can be distinct due to the independent approximations of $\boldsymbol{\phi}^h$ in $\Omega_e^{(+)}$ and $\Omega_e^{(-)}$.

To complete the discussion of the VMDG method, we reproduce from [1] the consistent linearization of (2):

$$
\begin{aligned}
K(\boldsymbol{\eta}_o^h, \Delta\boldsymbol{u}^h; \boldsymbol{\phi}^h) = {} & \underbrace{\int_{\tilde{\Omega}} \text{GRAD}\, \boldsymbol{\eta}_o^h : \mathbf{A}^h : \text{GRAD}\, \Delta\boldsymbol{u}^h \, \text{d}V}_{K0} + \underbrace{\int_{\tilde{\Gamma}_I} [\![\boldsymbol{\eta}_o^h]\!] : \left(\boldsymbol{\tau}_s \cdot [\![\Delta\boldsymbol{u}^h]\!] \right) \, \text{d}A}_{K1} \\
& - \underbrace{\int_{\tilde{\Gamma}_I} [\![\boldsymbol{\eta}_o^h]\!] : \left\{ \text{GRAD}\, \Delta\boldsymbol{u}^h : \mathbf{A}^h \right\} \, \text{d}A}_{K2} - \underbrace{\int_{\tilde{\Gamma}_I} \left\{ \text{GRAD}\, \boldsymbol{\eta}_o^h : \mathbf{A}^h \right\} : [\![\Delta\boldsymbol{u}^h]\!] \, \text{d}A}_{K3} \\
& - \underbrace{\int_{\tilde{\Gamma}_I} \left\{ \text{GRAD}\, \boldsymbol{\eta}_o^h : \boldsymbol{\Xi}^h : \text{GRAD}\, \Delta\boldsymbol{u}^h \right\} \cdot [\![\boldsymbol{\phi}^h]\!] \, \text{d}A}_{K4}
\end{aligned}
\tag{8}
$$

where $\Delta\boldsymbol{u}^h$ is the incremental displacement field. Expression (8) leads to the tangent stiffness matrix to be employed within the Newton–Raphson iterative procedure for solving the nonlinear weak form (2).

Remark. By employing (8) within the Newton–Raphson solution procedure, a quadratic rate of convergence of the out-of-balance force vector has been observed [1].

The terms in (8) have also been labeled with numbers corresponding to the "parent" terms in the weak form (2). We wish to call the reader's attention to the additional term $K4$ that involves the sixth-order tensor of material moduli $\boldsymbol{\Xi}^h$, defined

in [1,8] as: $\boldsymbol{\Xi}^h = \partial^2 \boldsymbol{P}^h / \partial \boldsymbol{F} \partial \boldsymbol{F}$. The appearance of this so-called unusual term is a consequence of the nonlinear dependence of $\mathbf{A}^h$ on the deformation gradient $\boldsymbol{F}$:

$$\begin{aligned} \mathrm{D}_{\phi^{(\alpha)}} \left[\left\{ \mathrm{GRAD}\, \boldsymbol{\eta}_o^h : \mathbf{A}^h \right\} \cdot \left[\!\left[\boldsymbol{\phi}^h \right]\!\right] \right] \cdot \Delta \boldsymbol{u}^{h(\alpha)} &= \left\{ \mathrm{GRAD}\, \boldsymbol{\eta}_o^h : \mathbf{A}^h \right\} \cdot \mathrm{D}_{\phi^{(\alpha)}} \left[\left[\!\left[\boldsymbol{\phi}^h \right]\!\right] \right] \cdot \Delta \boldsymbol{u}^{h(\alpha)} \\ &\quad + \left\{ \mathrm{GRAD}\, \boldsymbol{\eta}_o^h : \left(\mathrm{D}_{\phi^{(\alpha)}} \left[\mathbf{A}^h \right] \cdot \Delta \boldsymbol{u}^{h(\alpha)} \right) \right\} \cdot \left[\!\left[\boldsymbol{\phi}^h \right]\!\right] \\ &= \left\{ \mathrm{GRAD}\, \boldsymbol{\eta}_o^h : \mathbf{A}^h \right\} \cdot \left[\!\left[\Delta \boldsymbol{u}^h \right]\!\right] + \left\{ \mathrm{GRAD}\, \boldsymbol{\eta}_o^h : \boldsymbol{\Xi}^h : \mathrm{GRAD}\, \Delta \boldsymbol{u}^h \right\} \cdot \left[\!\left[\boldsymbol{\phi}^h \right]\!\right] \end{aligned} \tag{9}$$

where the definition of the variational (Gateaux) derivative can be found e.g. in [20].

We briefly focus on the structure of the unusual term $K4$ and its contribution to the overall global stiffness matrix. This term contributes only to the block-diagonal of the interface element stiffness matrix and does not induce further coupling between $\Omega_e^{(+)}$ and $\Omega_e^{(-)}$, which can be seen by expanding (9):

$$\begin{aligned} \left\{ \mathrm{GRAD}\, \boldsymbol{\eta}_o^h : \boldsymbol{\Xi}^h : \mathrm{GRAD}\, \Delta \boldsymbol{u}^h \right\} &= \boldsymbol{\delta}_s^{(+)} \cdot \left(\mathrm{GRAD}\, \boldsymbol{\eta}_o^{h(+)} : \boldsymbol{\Xi}^{h(+)} : \mathrm{GRAD}\, \Delta \boldsymbol{u}^{h(+)} \right) \\ &\quad + \boldsymbol{\delta}_s^{(-)} \cdot \left(\mathrm{GRAD}\, \boldsymbol{\eta}_o^{h(-)} : \boldsymbol{\Xi}^{h(-)} : \mathrm{GRAD}\, \Delta \boldsymbol{u}^{h(-)} \right). \end{aligned} \tag{10}$$

In contrast, the terms $K2$ and $K3$, which are analogous to standard DG terms [2,3,21], involve a product of the jump and averaging operators, leading to cross terms between $\boldsymbol{\eta}_o^{h(+)}$ and $\Delta \boldsymbol{u}^{h(-)}$ as well as between $\boldsymbol{\eta}_o^{h(-)}$ and $\Delta \boldsymbol{u}^{h(+)}$. We also remark that the $K4$ term is driven by the inter-element deformation residual $\left[\!\left[\boldsymbol{\phi}^h \right]\!\right]$; recall that the continuum solution to (1) is such that $[\![\boldsymbol{\phi}]\!] = \mathbf{0}$ on $\tilde{\Gamma}_I$. Thus, the magnitude of $K4$ will be significantly reduced for problems in which the computed solution has very small jumps $\left[\!\left[\boldsymbol{\phi}^h \right]\!\right]$ along element boundaries. Therefore, because of its block-diagonal structure and residual-driven nature, the effect of the $K4$ term within the global stiffness matrix may be less significant compared to the other interface stiffness terms $K1$ through $K3$.

Remark. For small strain DG methods, the penalty term $K1$ is positive definite and the flux terms $K2$ and $K3$ are negative definite [2]. However, the unusual term is indefinite due to the general nature of the material tensor $\boldsymbol{\Xi}^h$ as well as the dependence on the sign of the deformation jump $\left[\!\left[\boldsymbol{\phi}^h \right]\!\right]$. For example, given a fixed $\boldsymbol{\Xi}^h$, the sign of $K4$ changes if the elements $\Omega_e^{(+)}$ and $\Omega_e^{(-)}$ are penetrating or separated in the deformed configuration. We do not closely investigate the impact of this observation in the present work, but we remark that all the numerical results herein as well as in [1] are highly stable across large strains and rotations.

Nonetheless, the evaluation of the unusual term $K4$ in (8) significantly increases the complexity of the VMDG method. In principle, a closed-form expression for the sixth-order material tensor $\boldsymbol{\Xi}^h$, which we term as the curvature tensor, can always be derived from a closed-form expression for the acoustic tensor $\mathbf{A}^h$ associated with a constitutive material model; an example for a neo-Hookean material is contained in [1]. However, such a derivation can be quite involved for more complex material models. In the case of von-Mises plasticity, the second variational derivative would be required for the radial return algorithm and the associated nonlinear kinematic tensors. Additionally, the implementation of the $K4$ term is somewhat non-standard and involves additional calculations at the element level, although a generic representation in the form of shape function derivatives and constitutive matrices $\left(\mathbf{B}^T \mathbf{D} \mathbf{B}\right)$ is possible by adopting the ideas presented in the appendix of [20].

Therefore, the primary motivation for the present efforts is to devise algorithmic modifications to the VMDG method in order to avoid evaluating the unusual term $K4$. While the original method contained in (2) and (8) produces accurate results in a stable and robust fashion for hyperelastic problems [1], such modifications would streamline the implementation of the method and also simplify the extension of method to generalized constitutive models. The various methods are discussed in Section 3 and then assessed through numerical test cases in Section 4.

Remark. The linearized weak form (8) is symmetric in terms of $\boldsymbol{\eta}_o^h$ and $\Delta \boldsymbol{u}^h$, which can be verified by recalling the symmetries of $\mathbf{A}^h$ and $\boldsymbol{\Xi}^h$ for hyperelasticity. Maintaining symmetry will be an important consideration when evaluating the proposed modifications to (2) and (8) in the following section.

Remark. The preceding developments have been presented in terms of kinematic and constitutive quantities associated with the reference configuration. An entirely equivalent set of expressions can be written for the current or spatial configuration, which may be more desirable from the standpoint of implementation. These expressions are contained in the appendix of [1].

3. Algorithmic modifications to VMDG method

As discussed at the end of Section 2, the VMDG method as originally proposed in [1] contains a term in the consistent tangent matrix involving the sixth-order curvature tensor $\boldsymbol{\Xi}^h$, which increases both the implementational effort and the

Table 1
Summary of interface terms and mathematical properties of VMDG method family.

Name	Residual	Tangent	Consistency			Tangent symmetry
			Variational	Adjoint	Algorithmic	
VMDG	$R1\,R2\,R3$	$K1\,K2\,K3\,K4$	Yes	Yes	Yes	Yes
VMDGs	$R1\,R2\,R3$	$K1\,K2\,K3$	Yes	Yes	No	Yes
IVMDG	$R1\,R2$	$K1\,K2$	Yes	No	Yes	No
IVMDGs	$R1\,R2$	$K1\,K2\,K3$	Yes	No	No	Yes
RVMDG	$R1\,R2\,\bar{R}_o3$	$K1\,K2\,\bar{K}_o3$	Yes	No	Yes	No
RVMDGs	$R1\,R2\,\bar{R}_o3$	$K1\,K2\,K3$	Yes	No	No	Yes

computational cost of the method. Therefore, we propose a series of approximations to (2) and (8) that require less effort to implement in existing codes, which are summarized in Table 1. For each algorithm, the labels $R\bullet$ and $K\bullet$ indicate the terms from the residual vector and tangent stiffness matrix, respectively, that are retained from (2) and (8). The original proposed method VMDG is listed first for comparison. Each member of this family of modified VMDG algorithms are described in greater detail in the following sections.

A comprehensive comparative analysis is conducted in Section 4 whereby the computational economy, accuracy, and robustness of each method is assessed through carefully designed numerical benchmark problems. In particular, three types of consistency will be quantitatively assessed: variational, adjoint, and algorithmic. By definition, variational consistency implies that the exact continuum solution $\boldsymbol{\phi}$ to (1) satisfies the Euler–Lagrange equations associated with the discrete weak form, namely that substituting $\boldsymbol{\phi}$ into the modified counterpart to (2) produces a zero residual for all weighting functions $\boldsymbol{\eta}_o^h$. Since variational consistency combined with stability are necessary and sufficient conditions for convergence of discrete approximations in the context of linear PDEs [22], we require that all of the proposed modifications remain variationally consistent. Adjoint or dual consistency means that the exact solution $\boldsymbol{\eta}_o$ of the dual problem associated with the (consistently) linearized weak form posed at the deformation $\boldsymbol{\phi}$ satisfies the counterpart to (8) for all incremental displacements $\Delta\boldsymbol{u}^h$. This property has important implications in the proofs of optimal L^2 convergence, a-posteriori error estimation, and inverse problems; see [2,23–25] and references therein for a precise definition and further discussions on these implications. Finally, a method possesses algorithmic consistency if the entire and un-altered incremental weak form obtained from applying the variational derivative to the corresponding nonlinear weak form is used to evaluate the stiffness matrix within the Newton–Raphson solution procedure. Loss of algorithmic consistency can significantly increase the number of iterations required to reduce the norm of the out-of-balance force vector to a specified tolerance, particularly due to the loss of asymptotically quadratic convergence rate for the Newton–Raphson algorithm [26,27].

Each of these consistency properties along with accuracy and computational costs will be key factors in determining the validity of the proposed algorithmic modifications.

Remark. As indicated in Table 1, the VMDG method is the only method currently investigated (aside from the classical continuous Galerkin method) that possesses all three types of consistency. These properties are verified numerically in Section 4.

Remark. As will become obvious in the following sections, the weak forms of the VMDG (2), IVMDG (13), and RVMDG (16) methods possess a similar form as existing approaches in the literature [3–5,8]. The distinguishing feature of the present developments is the use of consistently derived expressions (6) for the penalty tensor and numerical flux terms according to [1]. In certain aspects, the existing approaches may be viewed as subsets of the present proposed methods, obtained by restricting the definition of the weighting tensors to $\boldsymbol{\delta}_s^{(\alpha)} = \frac{1}{2}\boldsymbol{I}$ and the penalty tensor to $\boldsymbol{\tau}_s = (\epsilon/h)\,\boldsymbol{I}$ with ϵ as a free parameter. Therefore, the conclusions drawn in Section 4 concerning the family of VMDG methods can provide insight into the performance of these referenced methods as well.

3.1. VMDGs: neglecting $\boldsymbol{\Xi}^h$ in the linearized form

Since the higher order material moduli $\boldsymbol{\Xi}^h$ is the major cause for concern, an obvious approximation is to drop the calculation of this term from (8) when evaluating the tangent stiffness matrix. The resulting method is referred to as VMDGs, for which the residual vector and tangent matrix are obtained from the following (see Table 1 row 2):

$$\begin{aligned}\tilde{R}\left(\boldsymbol{\eta}_o^h;\boldsymbol{\phi}^h\right) = &\underbrace{\int_{\tilde{\Omega}} \mathrm{GRAD}\,\boldsymbol{\eta}_o^h : \boldsymbol{P}^h \,\mathrm{d}V}_{R0} + \underbrace{\int_{\tilde{\Gamma}_I} [\![\boldsymbol{\eta}_o^h]\!] : \left(\boldsymbol{\tau}_s \cdot [\![\boldsymbol{\phi}^h]\!]\right) \,\mathrm{d}A}_{R1} - \underbrace{\int_{\tilde{\Gamma}_I} [\![\boldsymbol{\eta}_o^h]\!] : \left\{\boldsymbol{P}^h\right\} \,\mathrm{d}A}_{R2} \\ &- \underbrace{\int_{\tilde{\Gamma}_I} \left\{\mathrm{GRAD}\,\boldsymbol{\eta}_o^h : \mathbf{A}^h\right\} : [\![\boldsymbol{\phi}^h]\!] \,\mathrm{d}A}_{R3} - \underbrace{\int_{\tilde{\Omega}} \boldsymbol{\eta}_o^h \cdot \rho_o \boldsymbol{f} \,\mathrm{d}V}_{F\Omega} - \underbrace{\int_{\tilde{\Gamma}_\sigma} \boldsymbol{\eta}_o^h \cdot \boldsymbol{T} \,\mathrm{d}A}_{F\Gamma} = 0\end{aligned} \tag{11}$$

$$\tilde{K}(\boldsymbol{\eta}_o^h, \Delta\boldsymbol{u}^h; \boldsymbol{\phi}^h) = \underbrace{\int_{\tilde{\Omega}} \text{GRAD}\ \boldsymbol{\eta}_o^h : \mathbf{A}^h : \text{GRAD}\ \Delta\boldsymbol{u}^h\ \text{d}V}_{K0} + \underbrace{\int_{\tilde{\Gamma}_I} [\![\boldsymbol{\eta}_o^h]\!] : \left(\boldsymbol{\tau}_s \cdot [\![\Delta\boldsymbol{u}^h]\!]\right)\ \text{d}A}_{K1}$$
$$- \underbrace{\int_{\tilde{\Gamma}_I} [\![\boldsymbol{\eta}_o^h]\!] : \left\{\text{GRAD}\ \Delta\boldsymbol{u}^h : \mathbf{A}^h\right\}\ \text{d}A}_{K2} - \underbrace{\int_{\tilde{\Gamma}_I} \left\{\text{GRAD}\ \boldsymbol{\eta}_o^h : \mathbf{A}^h\right\} : [\![\Delta\boldsymbol{u}^h]\!]\ \text{d}A}_{K3}. \tag{12}$$

The primary advantage of this approach is that (2) and (11) are identical, which implies that the discrete solutions obtained from VMDG and VMDGs are identical. Most significantly, this equivalence implies that variational and adjoint consistency along with the accuracy of the VMDG method are inherited by VMDGs. Additionally, from (12) we observe that the stiffness matrix remains symmetric.

However, disappearance of the $K4$ term from (12) implies that the VMDGs method is not algorithmically consistent, which may cause a drop in the observed convergence rate in the Newton–Raphson scheme from second to first order. The number of extra iterations required likely depends heavily upon the nonlinearity of the constitutive model, the domain geometry, as well as the loading and boundary conditions. We also recall from Section 2 that the $K4$ term is driven by the inter-element deformation residual $[\![\boldsymbol{\phi}^h]\!]$. Therefore, when the computed solution has very small inter-element jumps $[\![\boldsymbol{\phi}^h]\!]$, the effect of this term on the Newton–Raphson convergence rate should also be insignificant.

Remark. As an alternative to dropping the $K4$ term, the sixth-order tensor $\boldsymbol{\Xi}^h$ could be evaluated through numerical differentiation of the reference material moduli $\mathbf{C}^h$ in a manner exactly analogous to the technique presented by Miehe [28] for computing the material moduli from the second PK-stress tensor. However, this approach would require evaluating the stress and material moduli six additional times for every integration point for every interface segment in the mesh. Therefore, the user must weigh the trade-offs of increased element-level calculation time versus increasing the number of global Newton–Raphson iterations. The numerical results in Section 4 can serve as a reference for making an informed decision.

3.2. IVMDG and IVMDGs: incomplete interior penalty method

As a more substantial modification, a formulation analogous to the incomplete interior penalty Galerkin (IIPG) method [6,29] is obtained by dropping the symmetrizing term $R3$ altogether from the residual vector (2). The resulting method, abbreviated IVMDG, is the computationally simplest method considered in the present study (see Table 1 row 3):

$$\hat{R}\left(\boldsymbol{\eta}_o^h; \boldsymbol{\phi}^h\right) = \underbrace{\int_{\tilde{\Omega}} \text{GRAD}\ \boldsymbol{\eta}_o^h : \boldsymbol{P}^h\ \text{d}V}_{R0} + \underbrace{\int_{\tilde{\Gamma}_I} [\![\boldsymbol{\eta}_o^h]\!] : \left(\boldsymbol{\tau}_s \cdot [\![\boldsymbol{\phi}^h]\!]\right)\ \text{d}A}_{R1} - \underbrace{\int_{\tilde{\Gamma}_I} [\![\boldsymbol{\eta}_o^h]\!] : \left\{\boldsymbol{P}^h\right\}\ \text{d}A}_{R2}$$
$$- \underbrace{\int_{\tilde{\Omega}} \boldsymbol{\eta}_o^h \cdot \rho_o \boldsymbol{f}\ \text{d}V}_{F\Omega} - \underbrace{\int_{\tilde{\Gamma}_\sigma} \boldsymbol{\eta}_o^h \cdot \boldsymbol{T}\ \text{d}A}_{F\Gamma} = 0 \tag{13}$$

$$\hat{K}(\boldsymbol{\eta}_o^h, \Delta\boldsymbol{u}^h; \boldsymbol{\phi}^h) = \underbrace{\int_{\tilde{\Omega}} \text{GRAD}\ \boldsymbol{\eta}_o^h : \mathbf{A}^h : \text{GRAD}\ \Delta\boldsymbol{u}^h\ \text{d}V}_{K0} + \underbrace{\int_{\tilde{\Gamma}_I} [\![\boldsymbol{\eta}_o^h]\!] : \left(\boldsymbol{\tau}_s \cdot [\![\Delta\boldsymbol{u}^h]\!]\right)\ \text{d}A}_{K1}$$
$$- \underbrace{\int_{\tilde{\Gamma}_I} [\![\boldsymbol{\eta}_o^h]\!] : \left\{\text{GRAD}\ \Delta\boldsymbol{u}^h : \mathbf{A}^h\right\}\ \text{d}A}_{K2}. \tag{14}$$

Similar approaches have been adopted by other authors for developing finite strain DG methods for hyperelasticity [3] and plasticity [4]; note that these approaches employ the standard average definition for the numerical flux and a scalar penalty parameter in contrast to (4)–(6). The clear advantage of this algorithmic modification is the simplicity as well as the avoidance of specifying the "stress" of the weighting function. Except for a few references [1,8], in the context of nonlinear solid mechanics the symmetrizing term $R3$ has been avoided either through adopting a lifting operator approach [10,30] or by neglecting it [3,4,31]. Additionally, within the context of the linear PDEs, the IIPG method has been shown to possess enhanced stability properties [21,31] in comparison to the symmetric interior penalty Galerkin (SIPG) method, which corresponds to the VMDG method. Similar behavior was proven [32] for the related nonsymmetric interior penalty Galerkin (NIPG) method, in which the sign of the $R3$ term is switched to positive.

However, two major drawbacks arise as a consequence of dropping the symmetrizing term. The first is that the IVMDG method loses the property of adjoint consistency, which has been linked by other researchers to degraded solution accuracy and convergence in the L^2 norm [6,23,25]. This consequence will be investigated for the first time in the context of nonlinear solid mechanics in Section 4.2. As previously mentioned, the loss of L^2 optimality can be detrimental in the context of

inverse problems and a-posteriori error estimation of quantities of interest [23,24]. The second major consequence is that the consistent tangent matrix obtained from (14) is nonsymmetric, which increases the memory requirements for the method as well as necessitating the use of nonsymmetric direct or indirect solvers. Also, many solid mechanics finite element codes contain data-structures that are hard-coded for symmetric matrices; therefore, additional effort would be required to re-code these data-structures cost in order to accommodate the IVMDG method. However, this latter effect is less of a concern when solving problems involving certain plasticity or friction models which engender a nonsymmetric tangent matrix by default [3,4].

To address this secondary concern of the nonsymmetric stiffness matrix in the IVMDG method, we also propose adding back the symmetrizing term $K3$ to the tangent matrix in (14), resulting in the IVMDGs method (see Table 1 row 4):

$$\hat{K}_s(\boldsymbol{\eta}_o^h, \Delta\boldsymbol{u}^h; \boldsymbol{\phi}^h) = \tilde{K}(\boldsymbol{\eta}_o^h, \Delta\boldsymbol{u}^h; \boldsymbol{\phi}^h). \tag{15}$$

This modification requires negligible additional calculations because $K3$ is the transpose of the $K2$ stiffness term, which is already included within the IVMDG method. Also, symmetry is restored to the tangent stiffness matrix, which can be confirmed by examining the form of $\tilde{K}$ in (12). However, the price of this modification is the trade-off of symmetry for algorithmic consistency. Since the algorithmic tangent (12) does not correspond with the consistent tangent (14), the IVMDGs method results in a modified-Newton approach. Notice that $K3$ involves the product of GRAD $\boldsymbol{\eta}_o^{h(\alpha)}$ and $\Delta\boldsymbol{u}^{h(\alpha)}$ from both elements $\Omega_e^{(+)}$ and $\Omega_e^{(-)}$ across an interface, implying that the structure of $\tilde{K}$ and $\hat{K}$ are significantly different. The impact of adopting this modified-Newton approach on the number of iterations required to reduce the norm of the out-of-balance force vector to a specified tolerance during a sequence of large deformation load steps will be investigated in Section 4.

Remark. Other authors have reported in [21] that smaller values of the penalty parameter are permissible within the IIPG method compared to the SIPG method while still yielding stable numerical results. Such claims could also be extended by analogy to the methods IVMDG and VMDG studied herein. However, we will employ the same values for $\boldsymbol{\tau}_s$ and $\delta_s^{(\alpha)}$ across all the methods in Table 1 in order to retain a uniform standard across the numerical benchmark problems.

3.3. RVMDG, RVMDGs: reference configuration acoustic tensor $\bar{\mathbf{A}}_o^h$

The final method we consider involves a compromise between the VMDG and IVMDG methods whereby an approximation is applied to the acoustic tensor $\mathbf{A}^h$ in the $R3$ term. Rather than updating the tensor $\mathbf{A}^h$ at each load step and iteration, a substitute tensor $\bar{\mathbf{A}}_o^h$ is evaluated once in the reference configuration $\boldsymbol{F} = \mathbf{1}$ and then kept frozen during the simulation process. This idea was previously proposed by Nguyen et al. [5] in the context of a DG approach for weakly enforcing the continuity requirements of a second-order homogenization scheme. By freezing the acoustic tensor, the numerical flux in $R3$ no longer depends on the deformation gradient, and the unusual term vanishes from the linearization in (9). The resulting algorithmic modification is termed as the reference Discontinuous Galerkin (RVMDG) method and can be expressed as follows:

$$\begin{aligned}\bar{R}\left(\boldsymbol{\eta}_o^h; \boldsymbol{\phi}^h\right) \;=\; & \underbrace{\int_{\tilde{\Omega}} \text{GRAD}\, \boldsymbol{\eta}_o^h : \boldsymbol{P}^h \, \mathrm{d}V}_{R0} + \underbrace{\int_{\tilde{\Gamma}_I} [\![\boldsymbol{\eta}_o^h]\!] : \left(\boldsymbol{\tau}_s \cdot [\![\boldsymbol{\phi}^h]\!]\right) \, \mathrm{d}A}_{R1} - \underbrace{\int_{\tilde{\Gamma}_I} [\![\boldsymbol{\eta}_o^h]\!] : \{\boldsymbol{P}^h\} \, \mathrm{d}A}_{R2} \\ & - \underbrace{\int_{\tilde{\Gamma}_I} \left\{\text{GRAD}\, \boldsymbol{\eta}_o^h : \bar{\mathbf{A}}_o^h\right\} : [\![\boldsymbol{\phi}^h]\!] \, \mathrm{d}A}_{\bar{R}_o 3} - \underbrace{\int_{\tilde{\Omega}} \boldsymbol{\eta}_o^h \cdot \rho_o \boldsymbol{f} \, \mathrm{d}V}_{F\Omega} - \underbrace{\int_{\tilde{\Gamma}_\sigma} \boldsymbol{\eta}_o^h \cdot \boldsymbol{T} \, \mathrm{d}A}_{F\Gamma} = 0 \end{aligned} \tag{16}$$

$$\begin{aligned}\bar{K}(\boldsymbol{\eta}_o^h, \Delta\boldsymbol{u}^h; \boldsymbol{\phi}^h) \;=\; & \underbrace{\int_{\tilde{\Omega}} \text{GRAD}\, \boldsymbol{\eta}_o^h : \mathbf{A}^h : \text{GRAD}\, \Delta\boldsymbol{u}^h \, \mathrm{d}V}_{K0} + \underbrace{\int_{\tilde{\Gamma}_I} [\![\boldsymbol{\eta}_o^h]\!] : \left(\boldsymbol{\tau}_s \cdot [\![\Delta\boldsymbol{u}^h]\!]\right) \, \mathrm{d}A}_{K1} \\ & - \underbrace{\int_{\tilde{\Gamma}_I} [\![\boldsymbol{\eta}_o^h]\!] : \left\{\text{GRAD}\, \Delta\boldsymbol{u}^h : \mathbf{A}^h\right\} \, \mathrm{d}A}_{K2} - \underbrace{\int_{\tilde{\Gamma}_I} \left\{\text{GRAD}\, \boldsymbol{\eta}_o^h : \bar{\mathbf{A}}_o^h\right\} : [\![\Delta\boldsymbol{u}^h]\!] \, \mathrm{d}A}_{\bar{K}_o 3}. \end{aligned} \tag{17}$$

This method retains more closely the appearance of the VMDGs method from Section 3.1 while also removing the effect of the unusual term $K4$. In particular, the symmetrizing terms $R3$ and $K3$ have been replaced with counterparts $\bar{R}_o 3$ and $\bar{K}_o 3$ evaluated in terms of the reference material moduli $\bar{\mathbf{A}}_o^h$. Thus, the element-level calculations and the implementational cost of the RVMDG method are reduced compared to the VMDG method. However, like the IVMDG method, the consistent tangent matrix (17) obtained from linearizing (16) is again nonsymmetric. The numerical results from Section 4.2 also indicate that the RVMDG method does not possess adjoint consistency. Therefore, the drawbacks of additional memory burden and the loss of L^2 optimality attributed to the IVMDG method also apply in the present case. Another possible concern

with (16) centers upon the fixed material tensor $\bar{\mathbf{A}}_o^h$. In the presence of large deformations, this reference configuration approximation may reduce the accuracy of the physical response that is computed from (16). One possible alternative would be to replace $\bar{\mathbf{A}}_o^h$ with the acoustic tensor $\tilde{\mathbf{A}}_n^h$ evaluated in terms of the deformation field $\boldsymbol{\phi}_n^h$ obtained at the previous converged load step. While this adjustment would make (16) more closely aligned with the current deformed state, the use of $\tilde{\mathbf{A}}_n^h$ engenders a step size dependence on the computed solution history, which may be undesirable. Also, the issues of symmetry and adjoint consistency are not repaired through this modification. Finally, employing the tensor $\mathbf{A}^h$ evaluated at the current iteration of the Newton–Raphson method amounts to the VMDGs method, which is considered within the present investigations.

Similar to the symmetrized counterpart to the IVMDG method proposed in Section 3.2, the term $\bar{K}_o 3$ in (17) may be replaced with $K3$ to arrive at a symmetrized method termed as the RVMDGs method:

$$\bar{K}_s(\boldsymbol{\eta}_o^h, \Delta\boldsymbol{u}^h; \boldsymbol{\phi}^h) = \tilde{K}(\boldsymbol{\eta}_o^h, \Delta\boldsymbol{u}^h; \boldsymbol{\phi}^h). \tag{18}$$

As before, the term $K3$ can be obtained simply as the transpose of $K2$, thereby minimizing the additional element-level calculations compared to (17). In fact, (18) is slightly less expensive to evaluate than (17) by avoiding the computation of $\bar{K}_o 3$. However, the possible deficiencies regarding the introduction of a modified tangent matrix in the context of the IVMDGs method apply to the present case as well, namely the reduced convergence rate of the modified-Newton algorithm.

4. Numerical results

In this section, the attributes of each modified DG method proposed in Table 1 of Section 3 are quantitatively assessed through a series of four carefully designed benchmark problems of increasing complexity. These problems represent a range of geometric, deformational, and material features often encountered in engineering applications. The properties to be assessed include: (i) variational consistency; (ii) adjoint consistency; (iii) algorithmic consistency; (iv) stability and robustness; (v) accuracy; (vi) element-level calculation cost; and (vii) domain-level iteration cost (related to algorithmic consistency). Both the implementational cost and the costs related to symmetry of the tangent stiffness matrix have been treated for each method. Emphasis is placed upon examples with closed-form solutions to facilitate exact quantification of accuracy. In particular, this enables the mathematical properties of the modified formulations in Section 3 to be assessed in a similar manner as the original formulation according to [1].

For all problems except for the anisotropic tension problem in Section 4.4, the material model employed is an isotropic neo-Hookean model of the following form:

$$\Psi(\boldsymbol{F}) = \frac{1}{2}\mu\left(\mathrm{tr}\left(\boldsymbol{F}^T\boldsymbol{F}\right) - 3\right) - \mu \ln J + \frac{1}{2}\lambda (J-1)^2 \tag{19}$$

where μ and λ are the Lamé parameters and $J = \det \boldsymbol{F}$. Expressions for the material tensors $\boldsymbol{P}$, $\mathbf{A}$, and $\boldsymbol{\Xi}$ associated with this model are presented in [1]. All two-dimensional problems are solved assuming plane strain conditions.

All computations were performed using a serial finite element code. The convergence criterion for the Newton–Raphson solver was specified as $\|R_i\|/\|R_o\| < 10^{-12}$, where $\|R_i\|$ and $\|R_o\|$ are the l^2 (Euclidean) norms of the out-of-balance force vector at the current and initial iteration, respectively. This tight relative tolerance was selected in order to sufficiently minimize algebraic error in the computed solutions and also to provide a uniform metric for assessing the six DG methods. Additionally, direct factorization of the stiffness matrix was employed in the Newton–Raphson algorithm for all cases. Numerical integration of the element interior terms $R0$ and $K0$ was performed using Gauss quadrature of sufficient order to fully integrate the polynomial shape functions of the corresponding element.

The various bubble functions representing the fine-scale models for evaluating the stability tensors $\boldsymbol{\tau}_s^{(\alpha)}$ are listed in Tables 2 and 3. The element types are designated first by shape according to the letter and second by number of nodes. Note that the bubble functions for wedges are applied only for the nonconforming interface segments in Section 4.3.2. The fine-scale bubble functions have been designed to be sufficiently higher-order compared to the coarse-scale functional space (either linear or quadratic) and to satisfy the requisite property that they vanish along all boundaries of the interface sector $\omega_s^{(\alpha)}$ except along the interface segment γ_s [17]. We have selected these particular fine-scale bubbles so that the computed values of the stability tensors $\boldsymbol{\tau}_s^{(\alpha)}$ remain close to those obtained using so-called residual-free bubbles [33]. While residual-free bubbles represent a higher-fidelity fine-scale modeling procedure, polynomial bubble functions greatly simplify the evaluation of the stability tensors $\boldsymbol{\tau}_s^{(\alpha)}$ in the computational setting. Additionally, we adopt the truncated sector approach proposed in [17] and augmented in [1] for determining the region of support $\omega_s^{(\alpha)} \subseteq \Omega_e^{(\alpha)}$ for the fine-scale bubble functions. The parametric coordinates (ξ, η, ζ) listed in the tables are referred to the local coordinate system defined over the truncated sector, which coincides with the parent element coordinate system only when $\omega_s^{(\alpha)} = \Omega_e^{(\alpha)}$. The reader is referred to [1,17] for a detailed explanation of the fully automatic procedure for determining $\omega_s^{(\alpha)}$.

Standard Gauss quadrature rules are employed for computing all interface-related integrals; the number of points used in each rule is listed in Tables 2 and 3. The third column refers to boundary or segment integrals, e.g. those in (2), while the fourth column refers to the sector integral contained in expression (7) for the stability tensors $\boldsymbol{\tau}_s^{(\alpha)}$. Also, the evolution

Table 2
Edge bubble functions employed for stability tensors $\boldsymbol{\tau}_s^{(\alpha)}$, two dimensions.

Element	Bubble function	Edge rule	Area rule
T3	$4\xi\,(1-\xi-\eta)$	3	4
Q4	$\frac{1}{2}\left(1-\xi^2\right)(1-\eta)$	3	9
T6	$16\xi\,(1-\xi-\eta)\,(1-\xi)\,(\xi+\eta)$	3	13
Q9	$\frac{1}{4}\left(1-\xi^4\right)(1-\eta)^2\,(2+\eta)$	3	16

Table 3
Face bubble functions employed for stability tensors $\boldsymbol{\tau}_s^{(\alpha)}$, three dimensions.

Element	Bubble function	Face rule	Volume rule
T4	$27\xi\eta\,(1-\xi-\eta-\zeta)$	3	4
W6	$\frac{27}{2}\xi\eta\,(1-\xi-\eta)\,(1-\zeta)$	3	6
B8	$\frac{1}{2}\left(1-\xi^2\right)\left(1-\eta^2\right)(1-\zeta)$	4	8
T10	$\left(\frac{81}{80}\right)^3\left[1-(2\xi-1)^4\right]\left[1-(2\eta-1)^4\right]\left[1-(2\,(1-\xi-\eta-\zeta)-1)^4\right]$	7	24
B27	$\frac{1}{2}\left(1-\xi^4\right)\left(1-\eta^4\right)(1-\zeta)^2\,(2+\zeta)$	9	27

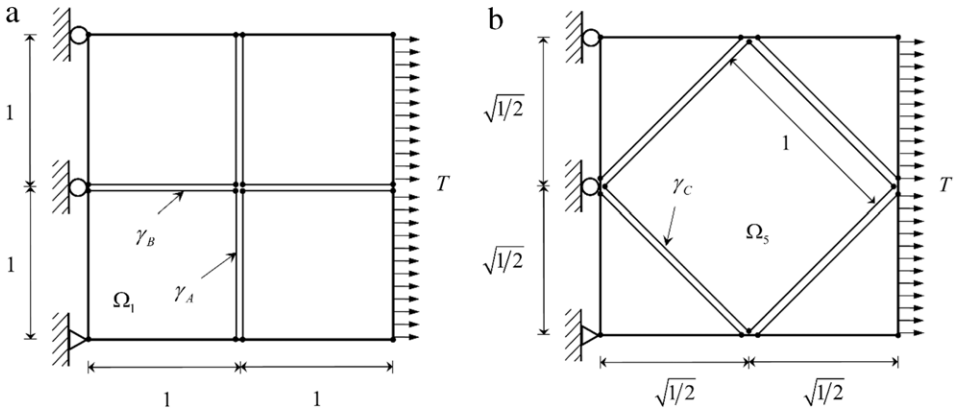

Fig. 2. Discontinuous Galerkin meshes for tensile test: (a) four Q4 elements; (b) one Q4 element oriented at 45°.

of the stability tensors $\boldsymbol{\tau}_s^{(\alpha)}$ during the Newton–Raphson iterations can degrade the observed convergence rate since their contributions to the consistent linearization are ignored. Therefore, as proposed in [1], the values of $\boldsymbol{\tau}_s^{(\alpha)}$ are updated only during the first three iterations and subsequently kept frozen during the remaining iterations of a load step.

4.1. Tensile patch test

The first problem consists of a square domain that is loaded by a tensile traction on the right face, as shown in Fig. 2. Two meshes are considered: one containing four bilinear quadrilateral elements and one containing a single quadrilateral surrounded by four triangular elements. In both cases, DG treatment is applied between each of the element interfaces, resulting in a discontinuous discrete approximation. The material properties are $E = 100$ and $\nu = 0.25$ and the traction is $T = 10$. Both the VMDG and VMDGs methods are applied to solve this problem in one load step. Our objective for studying this problem is to verify variational consistency, demonstrate the residual-driven nature of the $K4$ term involving $\boldsymbol{\Xi}^h$, and investigate the evolution of $\boldsymbol{\tau}_s^{(\alpha)}$ from the reference to current configurations.

The computed displacement of the node in the upper-right corner is $\boldsymbol{u} = (0.19874, -0.067363)$ for the first mesh, which agrees exactly with the analytical solution that can be found through recourse to the material model (19). Also, the computed overlaps or gaps between the elements in both meshes are zero up to machine precision. These results indicate the variational consistency of the VMDG method.

We report the value of the l^2 norm of the residual vector for each iteration of the nonlinear solution procedure in Tables 4 and 5 for both the VMDG and VMDGs method. Recall that in the VMDGs method, the $K4$ term involving both $\boldsymbol{\Xi}^h$ and the inter-element jump $[\![\boldsymbol{\phi}^h]\!]$ is dropped. However, the linear finite element shape functions are capable of exactly representing a state of uniform tension, which happens to be the state of the computed domain during each iteration of the Newton–Raphson procedure. Therefore, the $K4$ identically vanishes because $[\![\boldsymbol{\phi}^h]\!] = \mathbf{0}$, and thus the VMDG and VMDGs iteration histories are indistinguishable. These results confirm that the effect of the $K4$ term is negligible for problems in $[\![\boldsymbol{\phi}^h]\!] \approx \mathbf{0}$. Additionally, quadratic convergence of the residual vector is evident in both Tables 4 and 5.

Table 4
Evolution of residual l^2 norm, four Q4 element mesh.

Iteration number	Absolute residual norm		Relative residual norm	
	VMDG method	VMDGs method	VMDG method	VMDGs method
1	5.2042771×10^{-1}	5.2042771×10^{-1}	1.0×10^{0}	1.0×10^{0}
2	1.7771327×10^{-3}	1.7771327×10^{-3}	3.4035332×10^{-3}	3.4035332×10^{-3}
3	1.5476954×10^{-8}	1.5476954×10^{-8}	2.9738341×10^{-8}	2.9738341×10^{-8}
4	$1.6178823 \times 10^{-14}$	$1.6105750 \times 10^{-14}$	$3.1086954 \times 10^{-14}$	$3.0946547 \times 10^{-14}$

Table 5
Evolution of residual l^2 norm, single Q4 element mesh.

Iteration number	Absolute residual norm		Relative residual norm	
	VMDG method	VMDGs method	VMDG method	VMDGs method
1	3.6799796×10^{-1}	3.6799796×10^{-1}	1.0×10^{0}	1.0×10^{0}
2	1.2566226×10^{-3}	1.2566226×10^{-3}	3.4147635×10^{-3}	3.4147635×10^{-3}
3	1.0943854×10^{-8}	1.0943853×10^{-8}	2.9738899×10^{-8}	2.9738899×10^{-8}
4	$2.4372275 \times 10^{-14}$	$1.8757708 \times 10^{-14}$	$6.6229375 \times 10^{-14}$	$5.0972315 \times 10^{-14}$

Table 6
Cartesian components of stability tensors $\boldsymbol{\tau}_s^{(+)}$, reference and current configurations.

Edge	Reference	Current
A	$\boldsymbol{\tau}_s^{(+)} = \begin{bmatrix} 3.2895 & 0.0000 \\ 0.0000 & 1.8939 \end{bmatrix} \times 10^{-3}$	$\boldsymbol{\tau}_s^{(+)} = \begin{bmatrix} 3.6315 & 0.0000 \\ 0.0000 & 1.8549 \end{bmatrix} \times 10^{-3}$
B	$\boldsymbol{\tau}_s^{(+)} = \begin{bmatrix} 1.8939 & 0.0000 \\ 0.0000 & 3.2895 \end{bmatrix} \times 10^{-3}$	$\boldsymbol{\tau}_s^{(+)} = \begin{bmatrix} 2.1690 & 0.0000 \\ 0.0000 & 3.3468 \end{bmatrix} \times 10^{-3}$
C	$\boldsymbol{\tau}_s^{(+)} = \begin{bmatrix} 2.5917 & 0.6978 \\ 0.6978 & 2.5917 \end{bmatrix} \times 10^{-3}$	$\boldsymbol{\tau}_s^{(+)} = \begin{bmatrix} 2.9276 & 0.7381 \\ 0.7381 & 2.9276 \end{bmatrix} \times 10^{-3}$

Table 7
Normal and tangential components of $\boldsymbol{\tau}_s^{(+)}$.

Edge	Configuration	Normal $\boldsymbol{N}^{(+)} \cdot \boldsymbol{\tau}_s^{(+)} \cdot \boldsymbol{N}^{(+)}$	Tangential $\boldsymbol{T}^{(+)} \cdot \boldsymbol{\tau}_s^{(+)} \cdot \boldsymbol{T}^{(+)}$	Cross $\boldsymbol{N}^{(+)} \cdot \boldsymbol{\tau}_s^{(+)} \cdot \boldsymbol{T}^{(+)}$
A	Reference	3.2895×10^{-3}	1.8939×10^{-3}	0.0000
A	Current	3.6315×10^{-3}	1.8549×10^{-3}	0.0000
B	Reference	3.2895×10^{-3}	1.8939×10^{-3}	0.0000
B	Current	3.3468×10^{-3}	2.1690×10^{-3}	0.0000
C	Reference	3.2895×10^{-3}	1.8939×10^{-3}	0.0000
C	Current	3.4595×10^{-3}	2.0411×10^{-3}	2.7053×10^{-4}

This problem also provides a setting to investigate the effect of element orientation on the computed stability tensors $\boldsymbol{\tau}_s^{(\alpha)}$. The Cartesian components of $\boldsymbol{\tau}_s^{(+)}$ for element Ω_1 computed along edges A and B in the four quadrilateral mesh along with edge C of element Ω_5 in the single quadrilateral mesh are provided in Table 6. Observe that while both Ω_1 and Ω_5 are square elements with unit dimensions, the orientation of the element affects the magnitude of the computed Cartesian components. To clarify this point, in Table 7 we also provide the normal component $\boldsymbol{N}^{(+)} \cdot \boldsymbol{\tau}_s^{(+)} \cdot \boldsymbol{N}^{(+)}$ and tangential component $\boldsymbol{T}^{(+)} \cdot \boldsymbol{\tau}_s^{(+)} \cdot \boldsymbol{T}^{(+)}$ of the tensors, in which $\boldsymbol{N}^{(+)}$ denotes the outward unit normal to the respective element edge and $\boldsymbol{T}^{(+)}$ denotes the tangential unit vector which is parallel to the edge. In the reference configuration, we clearly see that all three interface segments have identical components. Also, the cross terms values $\boldsymbol{N}^{(+)} \cdot \boldsymbol{\tau}_s^{(+)} \cdot \boldsymbol{T}^{(+)}$ are zero, as expected from the analytical expressions. However, the normal and tangential components are distinct. Therefore, while the interface segment orientation affects the Cartesian coordinates of the stability tensors and by extension the penalty parameter $\boldsymbol{\tau}_s$, the orientation does not impact the normal and tangential components. Finally, the values of the stability tensors clearly evolve from the reference to the current configuration due to the large deformation of the elements (20% elongation). Note that the deformed shape of element Ω_5 is a rhombus while element Ω_1 is a rectangle, which accounts for the appearance of a cross term for edge C in Table 7. We remark that the current configuration values in Tables 6 and 7 are computed from the final deformed state, not the second iteration as alluded to in the beginning of Section 4.

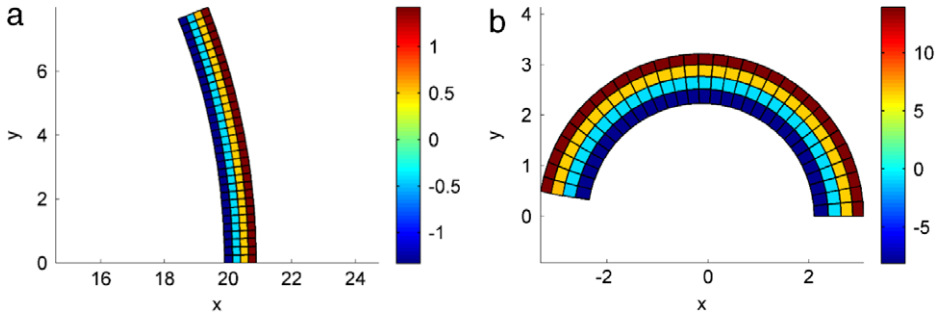

Fig. 3. Computed bending stresses $\sigma_{\theta\theta}$ on deformed configuration: (a) curvature $\psi = 22.5^\circ$; (b) curvature $\psi = 180^\circ$.

4.2. Pure bending of rectangular beam

The domain for this problem consists of an 8 unit long by 1 unit deep rectangular beam made of an elastic material with constants $E = 100$ and $\nu = 0.25$. The beam is bent from a straight, vertical configuration into a semi-circular shape in eight equal load steps with increments to the angle of curvature $\Delta\psi = 22.5^\circ$. Contours of the computed bending stress $\sigma_{\theta\theta}$ obtained from the VMDG method on a 4×32 linear quadrilateral element mesh are depicted in Fig. 3, where the origin of the cylindrical coordinate system is placed at the analytical center point for the subtended arc of the beam. The deformed configuration and the stress contours clearly illustrate the bending nature of this problem, which involves large strains and rotations of the elements. The exact solution for this problem is summarized in [1] and the references therein; the body force and surface tractions from this exact solution are applied as external loads in order to drive the computational model. Symmetry boundary conditions are applied to the lower edge of the beam, and the bottom point on the beam centerline is fixed in the horizontal direction to prevent rigid body motion.

We conduct a convergence rate study for this problem in order to evaluate the variational consistency, adjoint consistency, and accuracy properties of the proposed algorithmic modifications. All four element types are considered: triangles and quadrilaterals, linear and quadratic. The results from the VMDG, IVMDG, and RVMDG methods are benchmarked against the continuous Galerkin (CG) method using the same number of elements on uniform discretizations of the beam. The coarsest CG mesh for each element type contains 51 nodes (e.g. 2×16 linear quadrilateral elements), and uniform bisection is applied to obtain five levels of mesh refinement yielding meshes containing 33,345 nodes (64×512 elements). Diagonals for triangular meshes are oriented upper-left to lower-right. Each DG mesh is then formed directly from the skeleton of the corresponding CG mesh. However, the number of nodes for the DG meshes is equal to the number of elements times the number of nodes per element, which always exceeds the amount of the corresponding CG mesh. We mention again that the relative tolerance for the Newton–Raphson method is prescribed as $\|R_i\|_{l^2}/\|R_o\|_{l^2} < 10^{-12}$ to isolate discretization error from algebraic (solver) error.

The error norms between the displacement field of the exact and computed solution are evaluated at the load level $\psi = 22.5^\circ$ so that the results quickly reach the asymptotic convergence rates. Even so, from Fig. 3(a), the deformations are large enough such that elements at the top of the beam have moved horizontally by one entire edge length with respect to the bottom of the beam. In Fig. 4, the L_2 displacement error norms are recorded separately for each method grouped according to element type. We first focus on the convergence rates and then comment on accuracy. For linear elements, all methods converge at the optimal rate of 2.0 from the general theory of finite elements. However, we highlight in Fig. 4(c) and (d) that both the Incomplete DG and Reference DG methods exhibit suboptimal convergence rates for quadratic elements while the VMDG and CG methods attain the optimal rate of 3.0. This result clearly indicates that the IVMDG and RVMDG methods do not possess adjoint consistency. The dichotomy of the response from odd and even order element types has been observed by other authors in the context of linear PDEs and uniform meshes [6,25]. The present results are the first time this phenomenon has been presented for nonlinear solid mechanics. While the IVMDG and RVMDG methods still converge in the L^2 norm, the suboptimal rate has implications for inverse problems and error estimation [23] that the computational modeler should be aware of when selecting these methods.

For all element types in Fig. 4, we observe that the Variational Multiscale DG method is slightly more accurate than the CG method for the same number of elements, indicating that the element jumps increase the flexibility of the discrete model and its ability to represent the exact solution. Also, the coarsest mesh from the IVMDG method also possesses the same accuracy as the other methods for all element types for this problem; recall that the IVMDG method is less expensive than the VMDG method excluding the effect of the nonsymmetric stiffness matrix. However, the accuracy of the RVMDG method in Fig. 4(c) and (d) is one order magnitude lower compared to the other methods. Indeed, the results on the finest RVMDG mesh for T6 and Q9 elements is only slightly better than the solution on the coarsest mesh for the other three methods. Therefore, while all methods provide comparable accuracy for linear elements, the viability of the RVMDG method is significantly reduced by the poor quadratic element results.

Corresponding plots for the H^1 seminorm of displacement error are provided in Fig. 5. All of the methods exhibit uniform convergence at the optimal rates for each element type, namely rates near 1.0 for linear elements and 2.0 for quadratic

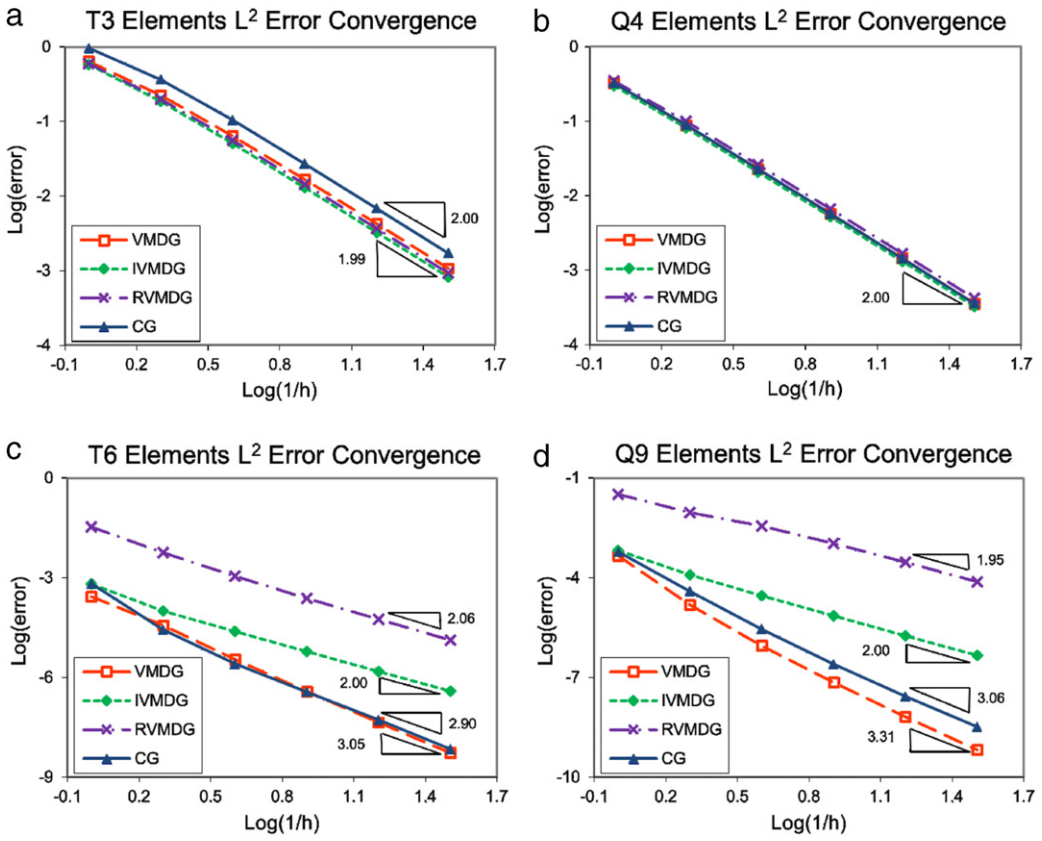

Fig. 4. Convergence rates of L^2 displacement error for CG and DG methods: (a) linear triangles; (b) linear quadrilaterals; (c) quadratic triangles; (d) quadratic quadrilaterals.

elements. These trends indicate that all the methods are variationally consistent. Similar to Fig. 4, the accuracy produced by all the methods is nearly equal except for the RVMDG method for quadratic elements.

Furthermore, for each DG method, we determined the maximum norm of the inter-element jumps $[\![\boldsymbol{\phi}^h]\!]$ across all integration points in a given mesh and report these values in Fig. 6. These quantities provide a measure of the amount of discontinuity introduced by the DG approximations. Note that the deformation field $\boldsymbol{\phi}$ is $\mathcal{O}(1)$ while the jumps are 4–5 magnitudes lower. Clearly, the jumps along inter-element boundaries are well controlled and converge toward zero upon mesh refinement.

As a final result for this problem, we provide further numerical proof that the stability tensors $\boldsymbol{\tau}_s^{(\alpha)}$ evolve with the deformation. In Fig. 7, the norm of the penalty parameter $\sqrt{\boldsymbol{\tau}_s : \boldsymbol{\tau}_s}$ at two load levels is plotted along each inter-element interface of the 4×32 linear quadrilateral mesh. The color of the edge indicates the value of the norm according to the associated legend. Comparing the trends in Fig. 7 with Fig. 3, we observe that the penalty tensor is larger in regions experiencing tensile stress at the outer radius and smaller in regions experiencing compressive stress at the inner radius, highlighting the effect of geometric stiffness on the stability tensors. We remark that the radial symmetry of the colors in Fig. 7(a) and (b) is a natural result from the computation of the stability tensors through (7) during the solution process; it is not a-priori injected into the system. Finally, the norm of the penalty tensor increases by about 20% in the tensile region with respect to the mean value of 4900; an equal but opposite change is evident in the compressive region near the inner radius.

Remark. Additional investigations of the evolution of the stability tensors $\boldsymbol{\tau}_s^{(\alpha)}$ are contained in Section 4.4 herein as well as in [1]. In this reference, the norm of the tensors was observed to remain bounded in the presence of indefinite or near-buckling material response.

4.3. Torsion of prismatic rod

4.3.1. Homogeneous rod

Consider a rod that is 4 units long and has a 1 unit square cross-section; the origin of coordinates is taken to be at the center of the bottom face. A torsional deformation is applied to the rod, expressed as follows:

$$\boldsymbol{\phi} = \begin{bmatrix} X\cos\theta - Y\sin\theta & X\sin\theta + Y\cos\theta & Z \end{bmatrix}^T, \qquad \theta(Z) = \frac{2\pi Z \psi}{L} \tag{20}$$

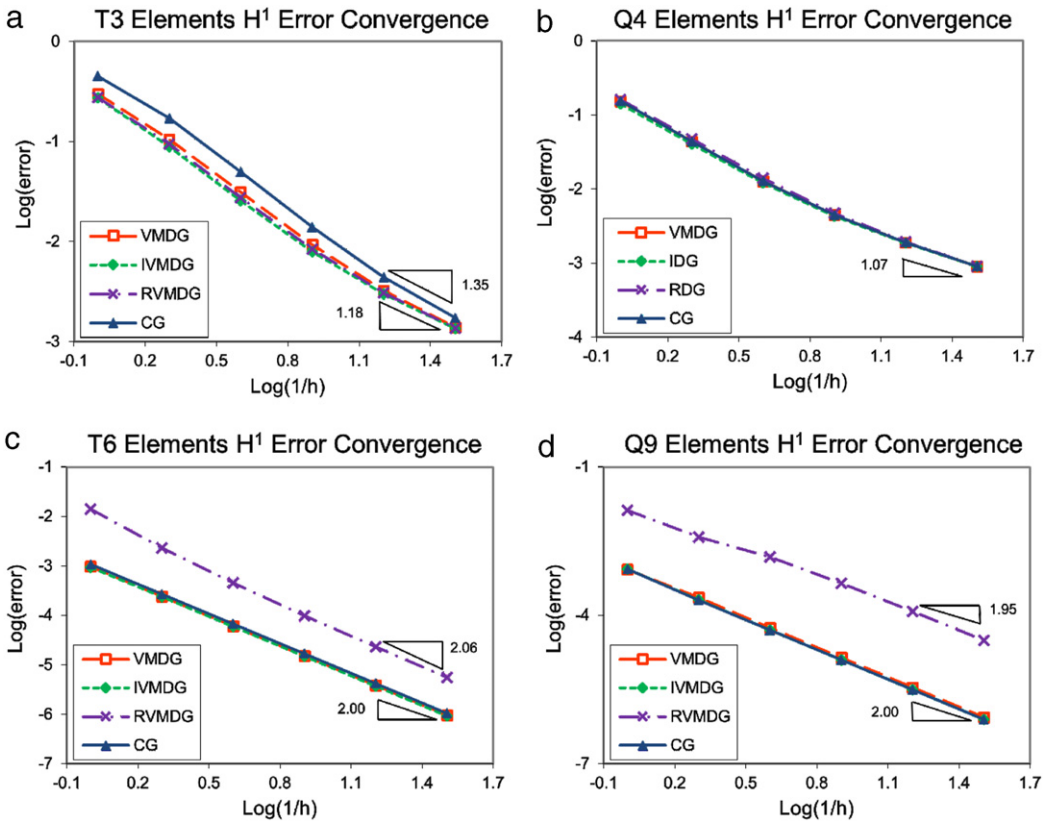

Fig. 5. Convergence rates of H^1 displacement error for CG and DG methods: (a) linear triangles; (b) linear quadrilaterals; (c) quadratic triangles; (d) quadratic quadrilaterals.

Table 8
Condition number of global tangent matrix for two load levels.

Twist	CG	VMDG	VMDGs	IVMDG	IVMDGs	RVMDG	RVMDGs
$\psi = 0.0$	1.06×10^4	6.99×10^4	6.99×10^4	7.03×10^4	6.99×10^4	6.99×10^4	6.99×10^4
$\psi = 2.0$	2.50×10^3	1.86×10^4	1.76×10^4	2.00×10^4	2.01×10^4	1.93×10^4	1.92×10^4

where $L = 4$ and ψ is the number of complete revolutions of the top face with respect to the bottom face. The rod is made of a neo-Hookean material with properties $E = 100$ and $\nu = 0.25$. For the following tests, the bottom face of the rod is fixed and the analytical tractions and body force derived from the deformation $\boldsymbol{\phi}$ and the constitutive law are applied to the other faces and to the domain; expressions for these forces are provided in [1]. Contour plots of the exact torsional stress field $\sigma_{z\theta}$ on the deformed rod are depicted in Fig. 8 for revolutions $\psi = 0.25$ and $\psi = 1.0$. The solution possesses a radially increasing shear stress analogous to the classical strength of materials solution for a circular rod under end torques. As is evident from the deformed states, this problem incorporates both significant rotational and straining effects.

For this numerical test, we quantitatively assess the following algorithmic properties of the proposed DG methods: global robustness and stability, algorithmic consistency (number of iterations), and computational cost at the element level. Each of the six methods discussed in Section 3 are investigated: VMDG, VMDGs, IVMDG, IVMDGs, RVMDG, and RVMDGs. A fixed, coarse mesh of $2 \times 2 \times 8$ trilinear hexahedral elements is employed for each simulation. As done previously, the uniform CG mesh is taken as the skeleton for defining the DG meshes, and a fully discontinuous approximation is applied with continuity weakly enforced between each element pair.

Before investigating the computational performance of the methods, we briefly highlight the condition number of the tangent stiffness matrix from each algorithm as an indicator of the relative conditioning of the formulations. These values are presented in Table 8 for the undeformed state $\psi = 0.0$ as well as for the last iteration of the Newton–Raphson algorithm at twist level $\psi = 2.0$ with load increment $\Delta\psi = 0.125$. In all cases, the condition numbers for the DG methods are less than one order greater than for the CG method, and the condition numbers are found to decrease as the twist is increased. Thus, all of the algorithms can be considered as well-conditioned.

We begin by comparing the computational time required to evaluate the element force vector and stiffness matrices emanating from (2) and (8) along with the corresponding expressions from the modified algorithms. The actual

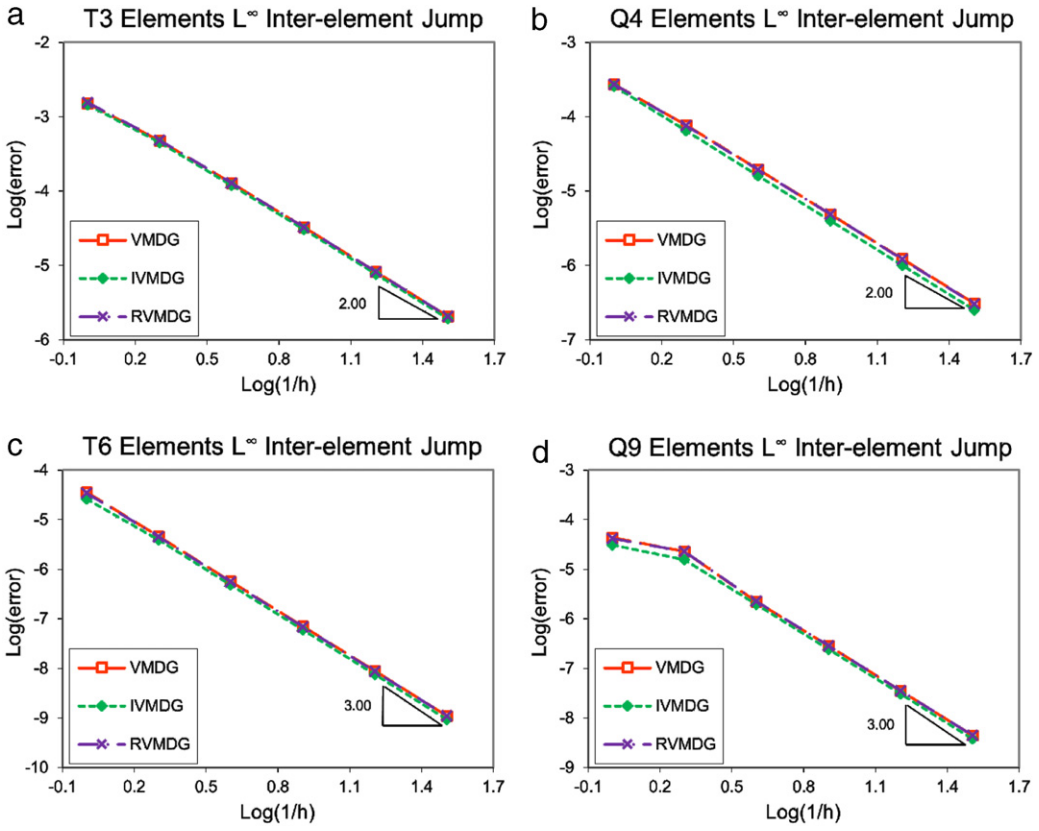

Fig. 6. Convergence rates of inter-element jumps $[\![\boldsymbol{\phi}^h]\!]$ for DG methods: (a) linear triangles; (b) linear quadrilaterals; (c) quadratic triangles; (d) quadratic quadrilaterals.

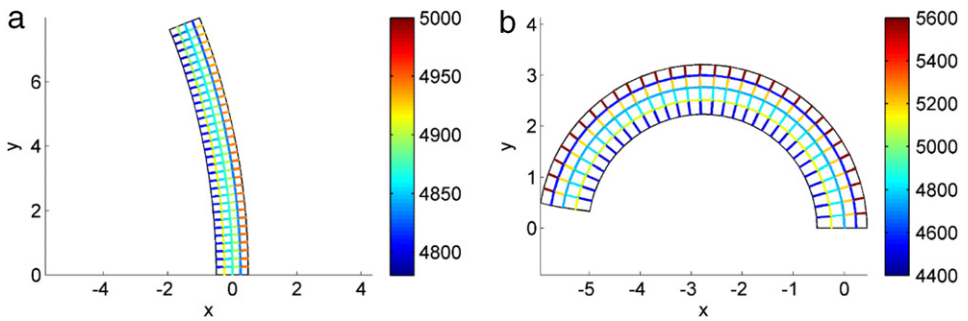

Fig. 7. Penalty tensor norm $\sqrt{\boldsymbol{\tau}_s : \boldsymbol{\tau}_s}$ from VMDG method along element interfaces: (a) curvature $\psi = 22.5°$; (b) curvature $\psi = 180°$. (For interpretation of the references to color in this figure legend, the reader is referred to the web version of this article.)

wall-time for evaluating these quantities depends on a number of factors: programming language, level of optimization of the matrix–vector product, CPU and machine properties, etc. Therefore, we aim to provide a relative comparison of the effort required to evaluate the interface terms $R1$–$R3$ and $K1$–$K4$ between each of the methods. To set a common metric for timing, each of the required matrices of shape functions and derivatives, $\boldsymbol{P}^h$, $\mathbf{A}^h$, $\boldsymbol{\tau}_s$, and $\delta_s^{(\alpha)}$ are precomputed at an integration point along a representative inter-element interface in the hexahedral mesh. For each method, these quantities are employed to repeatedly compute the associated residual vector and tangent matrix terms in Table 1, each for a total of 10,000 times. The total elapsed times are recorded in Fig. 9, normalized with respect to the baseline VMDG method. We observe that all of the other proposed DG methods require only 30%–40% of calculation time compared to the VMDG method. These savings are realized by avoiding the evaluation of the sixth-order tensor $\boldsymbol{\Xi}^h$ and the associated matrix multiplications in the $K4$ term. Also, the IVMDG method does not involve the evaluation of the $R3$ and $K3$ terms and therefore is the least expensive method at the element level. These cost savings at the element level translate to faster computation of the global force vector and stiffness matrix. Additionally, we emphasize that substantial implementational effort is saved by avoiding the derivation of $\boldsymbol{\Xi}^h$ from $\mathbf{A}^h$ employing tensorial calculus and continuum mechanics principles, as remarked in Section 3.

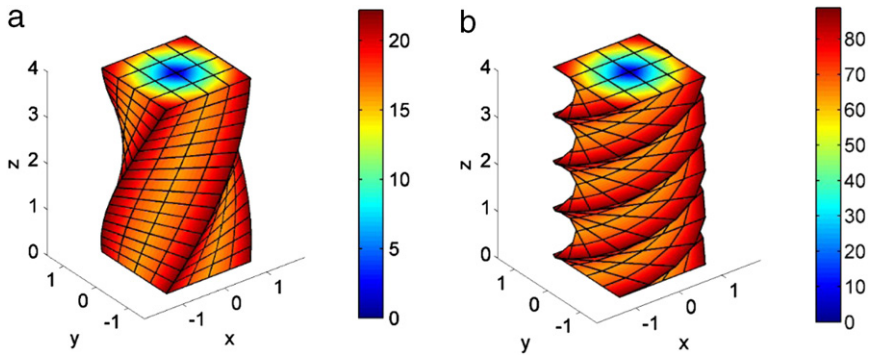

Fig. 8. Exact torsional stress $\sigma_{z\theta}$ on deformed configuration: (a) twist $\psi = 0.25$; (b) twist $\psi = 1.0$.

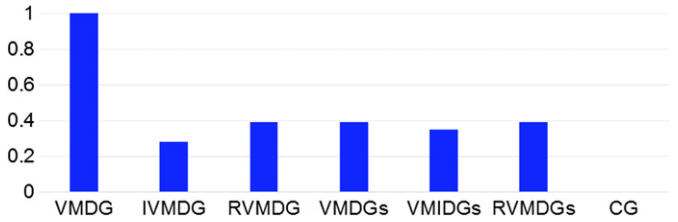

Fig. 9. Normalized wall-time to evaluate element force vector and stiffness matrix at an integration point.

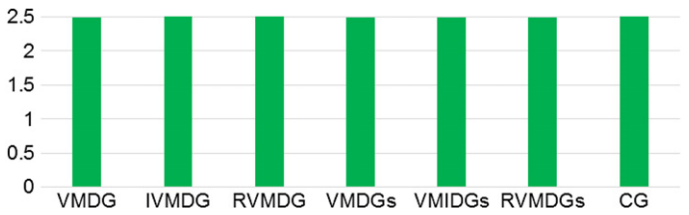

Fig. 10. Maximum twist factor ψ achieved by each method.

Next, a series of quasi-static simulations by each method are performed for the torsion problem whereby the twist factor ψ is increased from 0 in increments of $\Delta\psi = 0.125$. Recall that a uniform $2 \times 2 \times 8$ trilinear element mesh is employed for each case. The maximum twist factor achieved prior to divergence of the Newton–Raphson algorithm is shown in Fig. 10. All of the methods, including the classical CG method, are able to reach the value $\psi = 2.5$, which represents two and a half complete revolutions of the top face of the bar with respect to the bottom face. Thus, each of the methods are equally robust in terms of the level of deformation of the mesh sustained prior to divergence. In particular, we highlight that the use of the algorithmically inconsistent tangent matrices for the VMDGs, IVMDGs, and RVMDGs methods did not significantly limit the extent of deformation achieved.

Another key factor impacting the relative costs of the modified DG methods is the number of iterations required to reach a specified convergence tolerance during a load step of the nonlinear solution procedure. The number of iterations translates directly to the number of factorizations of the global stiffness matrix, an operation that scales as $\mathcal{O}\left(n^3\right)$ for direct solvers. Therefore, for large meshes, minimizing the number of Newton–Raphson iterations is crucial to maintain the competitiveness of overall numerical method. As an overview of the performance of the various proposed methods, in Fig. 11 we report the number of iterations required at three different load steps to reach a common convergence criterion of $\|R\| < 10^{-12}$. Each of the algorithmically consistent methods listed in Table 1, namely VMDG, IVMDG, and RVMDG, exhibit a uniform level of five iterations for each load step of the simulation. This performance indicates that they achieve quadratic rates of convergence analogous to the CG method.

In contrast, the symmetrized methods IVMDGs and RVMDGs required significantly more iterations to reach the same tolerance, approximately five times the other methods as seen in Fig. 11. Also, the behavior was less uniform across the load levels. Recall that these methods were designed to offset the extra memory and linear solver costs associated with the nonsymmetric consistent tangent matrices of the IVMDG and RVMDG methods. However, the poor performance of the nonlinear solution algorithm for the IVMDGs and RVMDGs methods indicates that the inclusion of the $K3$ term represents a significant perturbation to the consistent tangent matrix. The degraded convergence rate directly results in a substantially greater number of global linear equation solves, which is an added expense whether a direct or indirect solver is employed.

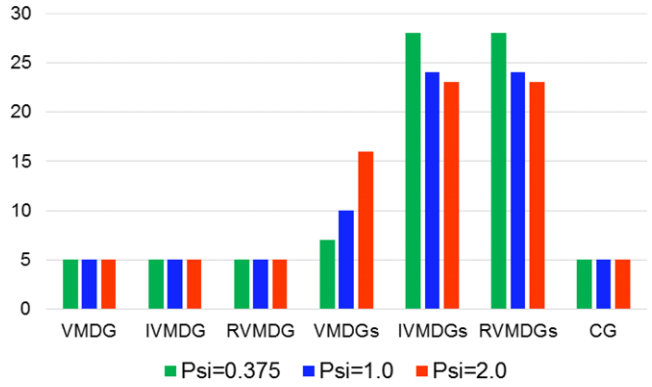

Fig. 11. Number of Newton–Raphson iterations for each method at load levels $\psi = 0.375$, $\psi = 1.0$, and $\psi = 2.0$.

Thus, the IVMDGs and RVMDGs methods are not economical alternatives when fully discontinuous approximations are employed.

The results for the VMDGs method represent a compromise between the quadratic convergence rate of the VMDG method and the suboptimal rate of the IVMDGs method. As evident in Fig. 11, only about 3–10 extra iterations are needed to reach the same converged solution as the VMDG method. Recall that the $K4$ term, which is neglected in the VMDGs method, is proportional to the inter-element jump $[\![\boldsymbol{\phi}^h]\!]$ and was determined to have a comparatively minor effect on the stiffness matrix in Section 4.1. Therefore, this method provides a reasonable tradeoff of paying for a few extra iterations while saving on the effort to evaluate the $\boldsymbol{\Xi}^h$ tensor and also retaining the other mathematical properties of the VMDG method demonstrated in Section 4.2.

Remark. The total run-time of a load step for each algorithm is a composite of the local element level calculations and number of global iterations as presented in Fig. 9 and Fig. 11, respectively. The actual wall time depends heavily upon the actual hardware and software platform and therefore is not reported. For example, on serial machines and small scale applications, the evaluation and assembly of the stiffness matrix may consume more time than the global factorization. In contrast, for large problems conducted on parallel computing architectures, the number of direct or indirect solves of the stiffness matrix is the primary computational cost. For the latter case, we point the reader to the remark at the end of Section 3.1 concerning the numerical evaluation of $\boldsymbol{\Xi}^h$. Such an approach would almost eliminate the extra Newton–Raphson iterations by restoring algorithmic consistency while avoiding the burden of implementing the sixth-order moduli tensor.

4.3.2. Bi-material rod

Next, we perform a secondary investigation of algorithmic consistency on a 4-unit long rod consisting of two sections placed end-to-end with distinct material moduli, $E = 400$ in the upper half and $E = 100$ in the lower half. The performance of the DG method for materials with disparate moduli is relevant to the modeling of interfacial response of fibrous composites [34]. As shown in [1], an exact solution for the composite rod can be manufactured by carefully appending the two solutions for the component sections through a rigid body rotation. Contour plots of the u_x displacement component on the deformed configuration at the load levels $\psi = 0.25$ and $\psi = 1.25$ are provided in Fig. 12, where the reduced twisting of the top section indicates the material mismatch. Here, ψ now refers to the number of revolutions of the mid-plane with respect to the rod's bottom face. Additionally, the superimposed mesh lines indicate that the discretization employed for this problem is intentionally nonconforming, where we have introduced bias in the edge spacing which is opposite in the upper and lower sections of the rod. The resulting discretization of the material interface is shown in Fig. 13 along with contours of the interface jump $[\![\boldsymbol{\phi}^h]\!]$ and magnitude of numerical flux vector at the load level $\psi = 0.375$. The gray lines and black lines represent edges from the faces of elements derived from the lower section and upper section of the rod, respectively. This nonconforming mesh necessitates special treatment of the interface between the materials; thus, we apply the proposed DG methods locally at this interface while employing continuous approximations with trilinear hexahedral elements in the interior of the rod sections. The highly disparate size of the interface sectors (varying from 75% to less than 1% of a given element face) along with the differing material moduli creates a significant challenge for the numerical method. Nonetheless, the consistently derived weighted numerical flux and stability tensors within the DG method as presented in Section 2 yield accurate and stable results for this problem, as seen in Fig. 13(a) and (b). We remark that the total numerical flux $\boldsymbol{\lambda}^h = \{\boldsymbol{P}^h\} + \boldsymbol{\tau}_s [\![\boldsymbol{\phi}^h]\!]$ is slightly over-predicted within the very small interface segments due to the somewhat larger values of the penalty tensor $\boldsymbol{\tau}_s$ computed in those regions compared to the larger interface segments. The difficulty of evaluating the interface stability parameters inside disparate-sized segments has also been a significant issue for embedded interface methods [19].

For this bi-material problem with localized DG treatment, we repeat the investigations from Section 4.3.1. The applied torsional tractions and body forces are increased through increments of $\Delta\psi = 0.0625$ to the loading parameter, and the maximum twist sustained prior to divergence of the Newton–Raphson algorithm is recorded in Fig. 14 for each DG method.

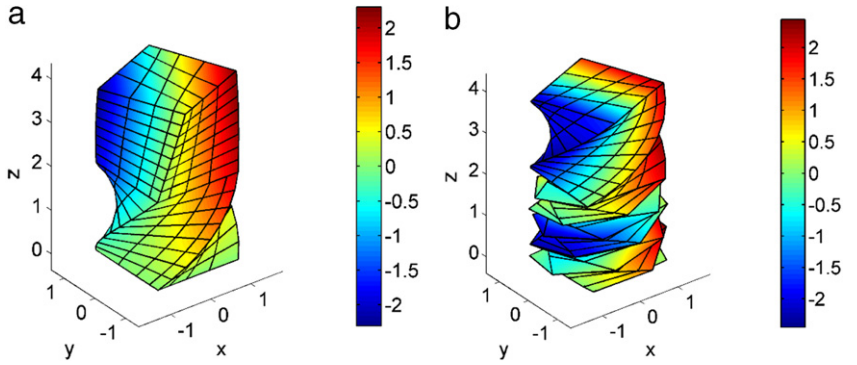

Fig. 12. Displacement u_x on deformed configuration of bi-material rod: (a) twist $\psi = 0.25$; (b) twist $\psi = 1.25$.

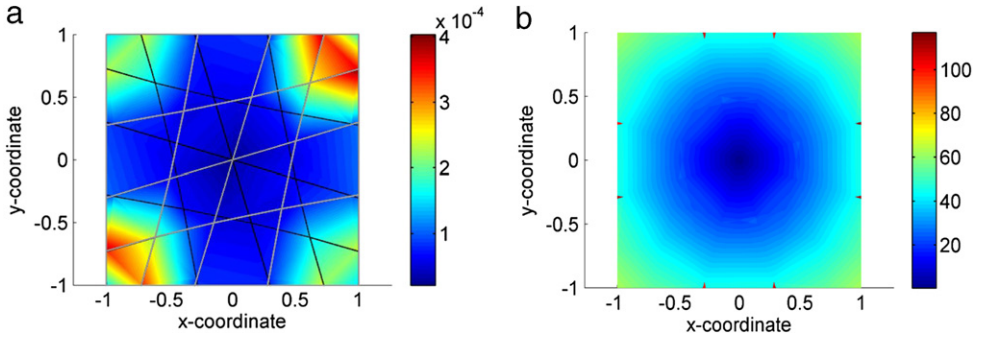

Fig. 13. Contour plots at material interface for twist $\psi = 0.375$: (a) magnitude of discrete interface gap $[\![\phi]\!]$; (b) magnitude of numerical flux vector.

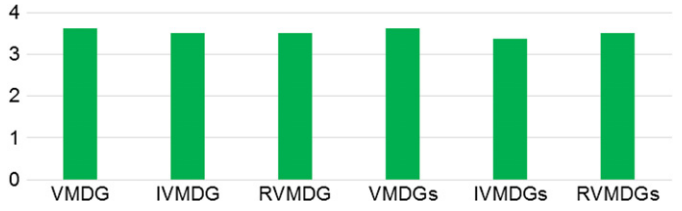

Fig. 14. Maximum twist factor ψ achieved by each method.

The results are again similar from each of the six DG methods, indicating a similar level of robustness. Note that two regions of $4 \times 4 \times 8$ elements have been utilized in the present case, which is a one level finer mesh compared to that employed in Section 4.3.1. Therefore, the maximum twist has also increased by nearly a factor of 2 as a reflection of the more flexible (and thus more accurate) finite element mesh.

The number of iterations required to reach convergence of the out-of-balance force vector is tabulated in Fig. 15 for different load levels. Similar trends are evident as compared to the results in Fig. 11 of Section 4.3.1 for the uniform material case and fully discontinuous approximations. Namely, the methods employing algorithmically modified tangent stiffness matrices (VMDGs, IVMDGs, and RVMDGs) require more iterations compared to their algorithmically consistent counterparts (VMDG, IVMDG, and RVMDG). However, the increase for each method (e.g. from IVMDG to IVMDGs) is much smaller for the present bi-material rod results in Fig. 15 compared to the uniform material rod in Fig. 11. This behavior makes sense when it is recognized that the modified interface stiffness terms affect only a small percentage of the global tangent matrix for localized interface problems, where the matrix is dominated by the continuous Galerkin contributions on the domain interior. In contrast, for fully discontinuous approximations, modifications to the interface segment stiffness matrices affect a majority of the terms in the global tangent matrix. Therefore, the IVMDGs and RVMDGs methods are viable options for problems in which the DG treatment is applied only to isolated nonconforming interfaces in an overall continuous Galerkin discretization. Recall that these methods realize a sizable memory savings and linear-equation solver time reduction by employing symmetric element tangent matrices.

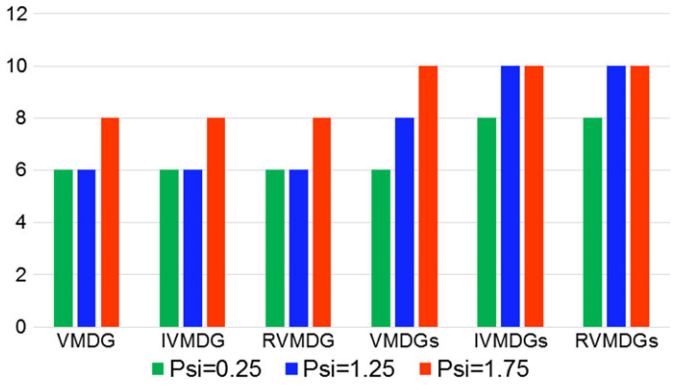

Fig. 15. Number of Newton–Raphson iterations for each method at load levels $\psi = 0.25$, $\psi = 1.25$, and $\psi = 1.75$.

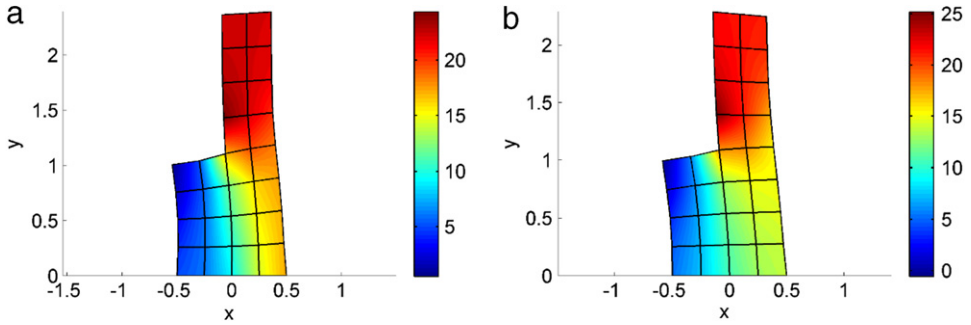

Fig. 16. Tensile stress σ_{yy} on deformed configuration, CG method, $E_f/E_m = 1.0$: (a) $\theta = 30°$; (b) $\theta = 60°$.

4.4. Anisotropic stair-step plate under tension

We now wish to assess whether the conclusions drawn about the algorithmic properties of the proposed methods in the context of isotropic materials and smooth loading carries over problem classes with anisotropic materials and less-regular solution fields. To this end, we apply the VMDGs, IVMDG, and IVMDGs methods to model the problem of a stair-step plate loaded in tension. The domain consists of a 1 mm wide by 2 mm long plate with a 0.5 mm $\times$ 1 mm rectangle cut out of the upper-left corner as shown in the contour plots in Fig. 16. The lower edge of the plate is fully-fixed, and a tensile traction of 5 MPa is applied along the top surface $Y = 2$ mm. The plate is assumed to be made of an anisotropic material given by the following strain–energy density function:

$$\Psi(\boldsymbol{C}) = C_1\left(\bar{I}_1(\boldsymbol{C}) - 3\right) + C_2\left(\bar{I}_1(\boldsymbol{C}) - 3\right)^2 + C_3\left(\bar{I}_1(\boldsymbol{C}) - 3\right)^3 + E_f/4\left(\bar{I}_4(\boldsymbol{C}, \boldsymbol{A}) - 3\right) + \kappa/2\,(J-1)^2 \tag{21}$$

where $\bar{I}_1(\boldsymbol{C}) \equiv \mathrm{tr}\left(\bar{\boldsymbol{C}}\right)$, $\bar{I}_4(\boldsymbol{C}, \boldsymbol{A}) = \boldsymbol{A}\cdot\bar{\boldsymbol{C}}\cdot\boldsymbol{A}$, and $\bar{\boldsymbol{C}} \equiv J^{-2/3}\boldsymbol{C}$; further references for the form of the stress tensor and material moduli are contained in [20]. The unit vector $\boldsymbol{A} = \begin{bmatrix}\cos\theta & \sin\theta & 0\end{bmatrix}^T$ indicates the orientation of reinforcing fibers within an underlying isotropic matrix represented through a Yeoh-type material model; the fiber angle θ is measured with respect to the X axis. The fiber orientation influences the characteristics of the deformed shape depending upon whether they are primarily aligned or perpendicular to the applied loading, as exhibited in Fig. 16(a) and (b). In the simulations that follow, we define the material parameters as: $E_m = 100$ MPa, $\nu = 0.35$, $G_m = E_m/2\,(1+\nu)$, $\kappa = E_m/3\,(1-2\nu)$, $C_1 = 0.5G_m$, $C_2 = -0.05G_m$, and $C_3 = 0.025G_m$.

We conducted a comprehensive numerical study of this problem employing the VMDGs, IVMDG, and IVMDGs methods as well as the CG method as a benchmark. Due to the relative complexity of the constitutive model (21), the VMDG method was not tested because it would require the evaluation of $\boldsymbol{\Xi} = \partial^3\Psi/\partial\boldsymbol{F}\partial\boldsymbol{F}\partial\boldsymbol{F}$. A family of 15 physical problems was generated from the parameter sets $E_f/E_m = \{0.1,\ 1.0,\ 10.0\}$ and $\theta = \{0°,\ 30°,\ 45°,\ 60°,\ 90°\}$. Each problem was simulated with all 4 methods using both linear quadrilateral and linear triangular elements on three levels of nested, uniform meshes; the coarsest Q4 mesh is illustrated in Fig. 16. For the case of DG meshes, fully discontinuous approximations were employed. The diagonals for the triangular meshes are oriented in a union-jack fashion. In all cases, the 5 MPa tensile traction was applied in a single load step; this magnitude was the largest load level for which the CG method was able to converge across all of the simulations. Highlights of the comprehensive results are presented below in order to assess the algorithmic properties of the proposed DG methods.

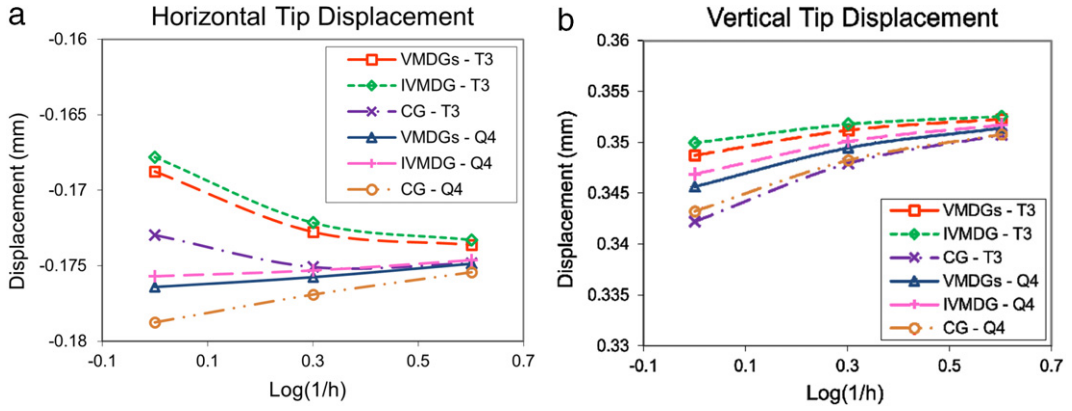

Fig. 17. Convergence of plate tip displacement, $\theta = 45^\circ$ and $E_f/E_m = 1.0$: (a) u_x displacement; (b) u_y displacement.

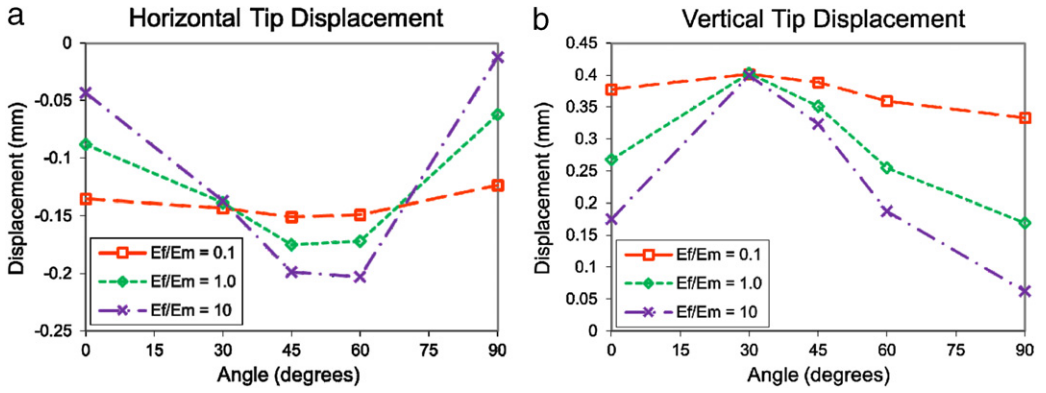

Fig. 18. Variation of tip displacement as a function of E_f/E_m and θ: (a) u_x displacement; (b) u_y displacement.

Remark. For increasing moduli ratio E_f/E_m, the deviation from isotropic constitutive response increases. Also, the orientation of the fibers with respect to the inter-element interfaces could have a significant effect on the ratio of normal to tangential components of the stability tensors. These effects are carefully investigated below.

We first present the convergence of the displacement values at the point $(X, Y) = (0.5, 2)$ obtained from a series of uniformly refined meshes in Fig. 17. A representative simulation with the material properties $\theta = 45^\circ$ and $E_f/E_m = 1.0$ is considered. All three methods and both element types demonstrate convergence toward a common value both for the horizontal and vertical components of displacement. Note that the IVMDGs results are not included because they exactly match the values from the IVMDG method, which is to be expected according to the discussion in Section 3.2. Also, in Fig. 17(b), the DG methods exhibit slightly higher accuracy than the CG method for both element types, which can be attributed to the flexibility afforded by the inter-element jumps that help to offset the constraining effect of the fully-fixed boundary condition. Other combinations of the material properties (fiber orientation and fiber moduli) produced convergent displacement results that exhibited similar trends amongst the CG and DG methods as exhibited by Fig. 17. We remark that while the tip displacement value is only 0.35 mm, the deformations are relatively large compared to the 2 mm length of the plate, justifying the use of finite strain kinematics.

In Fig. 18, we present the variation of the plate's tip displacement as a function of the changing material properties as obtained from the most-refined quadrilateral VMDGs meshes. Similar results are obtained from each of the other methods in accordance with the remarks on the preceding figure. As expected, the orientation of the fibers as well as their relative stiffness compared to the underlying isotropic matrix has a significant effect on the computed response. Only for the value $\theta = 30^\circ$ do the results indicate minimal variation of the tip deflection with respect to the moduli ratio. For small values of E_f, the tip displacement is nearly constant as the angle θ is adjusted, indicating that the isotropic material response dominates. In contrast, the stiffest response corresponds to $E_f/E_m = 10$ and $\theta = 90^\circ$ in which the reinforcing fibers are oriented in the direction of the tensile load; for this case, the displacements are 10 times smaller than for the softest case $E_f/E_m = 0.1$ and $\theta = 30^\circ$. Recall that the fibers are not discretely represented in the mesh but are rather accounted for within the anisotropic constitutive model (21). The significant variation in the computed response exhibited in Fig. 18 indicates that this problem provides for an extensive numerical test of the proposed DG methods across a range of constitutive behavior.

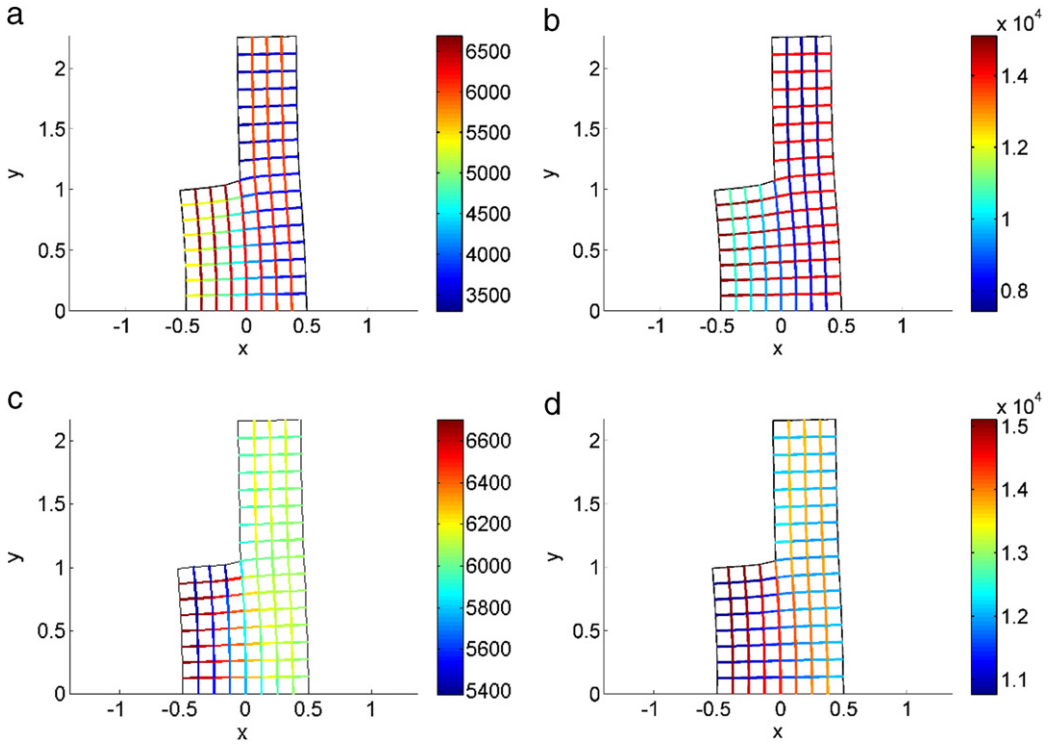

Fig. 19. Penalty tensor $\boldsymbol{\tau}_s$ components from VMDGs method along element interfaces: (a) $\tau_{nn}, \theta = 0°$; (b) $\tau_{tt}, \theta = 0°$; (c) $\tau_{nn}, \theta = 90°$; (d) $\tau_{tt}, \theta = 90°$.

This anisotropic material problem also serves to highlight the tensorial nature of the stability tensors in the proposed DG method. In Fig. 19, edge contour plots are provided for the components of the penalty tensor $\boldsymbol{\tau}_s$ obtained from the VMDGs method applied to the $E_f/E_m = 1.0$ case. The normal and tangential components are denoted by $\tau_{nn} = \boldsymbol{n} \cdot \boldsymbol{\tau}_s \cdot \boldsymbol{n}$ and $\tau_{tt} = \boldsymbol{t} \cdot \boldsymbol{\tau}_s \cdot \boldsymbol{t}$, respectively, where $\boldsymbol{n}$ is the normal unit vector and $\boldsymbol{t}$ is the tangential unit vector to the associated element interface in the deformed configuration. From Fig. 19(a) for the $\theta = 0$ case, we observe that the edges with unit normal $\boldsymbol{n}$ aligned with the fiber orientation $\boldsymbol{A}$ have a larger normal component τ_{nn} compared to perpendicularly oriented edges. The exact opposite is true in Fig. 19(b): the tangential component τ_{tt} is larger on edges with $\boldsymbol{t}$ parallel to $\boldsymbol{A}$. These features carry over into Fig. 19(c) and (d) by recognizing that the orientation vector $\boldsymbol{A}$ points vertically instead of horizontally. Thus, the VMDG method automatically accounts for material anisotropy by increasing the components of the penalty tensor in the preferential material direction. This feature is unique to the present method and is not shared by formulations with scalar-valued stability parameters. The effects of these tensorial weights and penalty terms on the computed results in general have yet to be fully investigated.

Remark. Note in Fig. 19 that the magnitude of the tangential component is about twice that of the normal component, which is the inverse of the trend observed for $\boldsymbol{\tau}_s^{(+)}$ in Section 4.1. This result agrees with the inverse relationship between $\boldsymbol{\tau}_s^{(+)}$ and $\boldsymbol{\tau}_s$ defined in (6).

Remark. We again emphasize that expressions (6), as derived from the fine-scale models, provide an automatic and robust definition for the DG stability tensors $\boldsymbol{\delta}_s^{(\alpha)}$ and $\boldsymbol{\tau}_s$ that account for evolving geometric and material nonlinearity. This automatic procedure frees the user from having to specify a fixed value of the stability parameters across the large spectrum of anisotropic material response.

Finally, the most important objective of this section is to determine whether the variations in material anisotropy have a significant effect on the algorithmic performance of the modified DG methods. The number of Newton–Raphson iterations required for convergence of each method is reported in Fig. 20 as a function of the anisotropic material parameters. All results are shown for the finest meshes; almost identical values were obtained on the coarser meshes except with less variation as a function of angle θ. For the IVMDG and CG methods, the number of iterations is nearly constant across all cases; only one or two extra iterations were needed for $E_f/E_m = 10$. The VMDGs method also exhibited fairly uniform performance, with variations of about 3–4 iterations for larger moduli ratios. Also, this method required only about 4–5 more iterations than the algorithmically consistent CG and IVMDG methods. However, the IVMDGs method again required significantly more iterations to reach convergence. Its performance also varied significantly with increasing anisotropy; in fact, the method was divergent for all cases with $E_f/E_m = 10$.

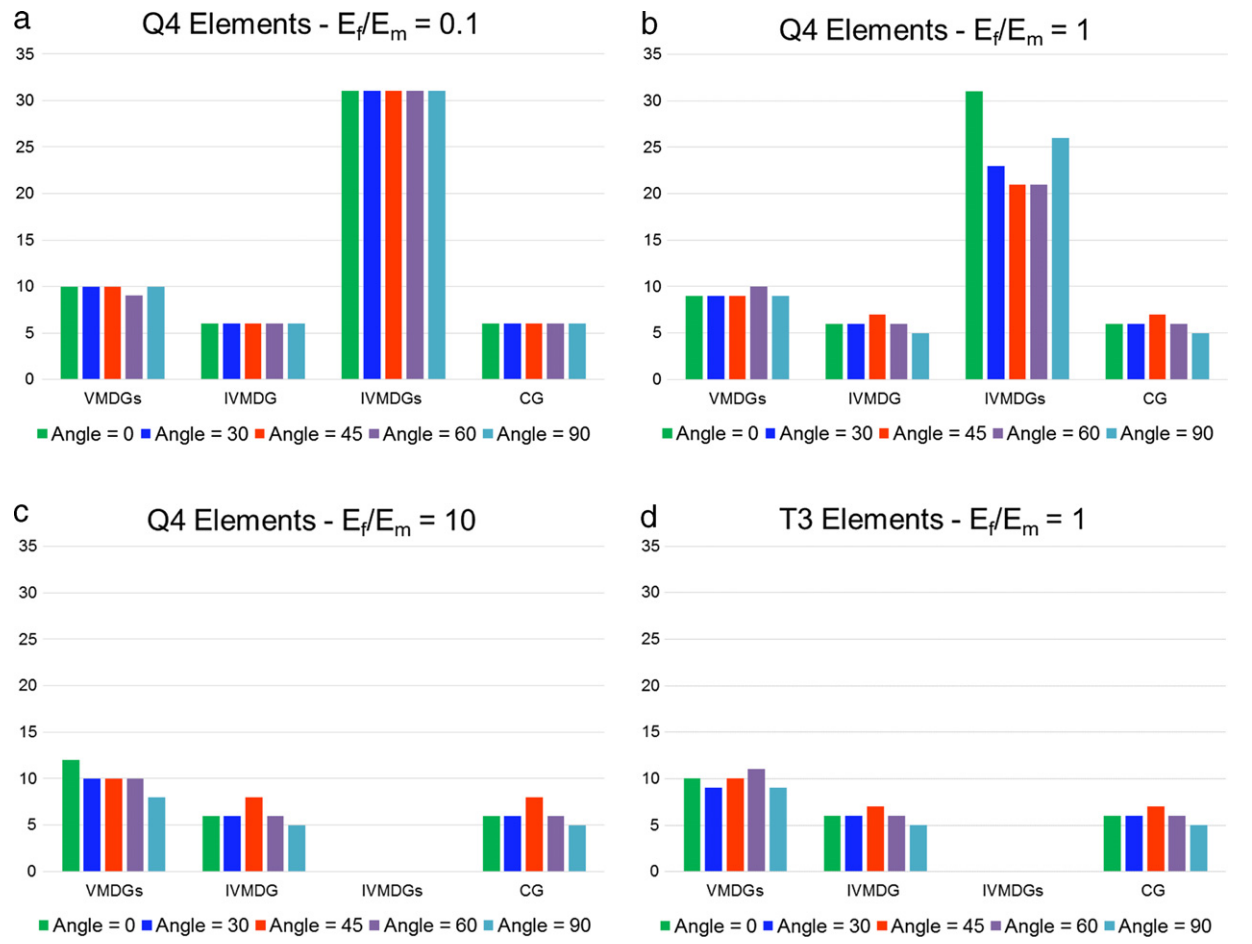

Fig. 20. Number of Newton–Raphson iterations for each method: (a) linear quadrilaterals, $E_f/E_m = 0.1$; (b) linear quadrilaterals, $E_f/E_m = 1.0$; (c) linear quadrilaterals, $E_f/E_m = 10$; (d) linear triangles, $E_f/E_m = 1.0$.

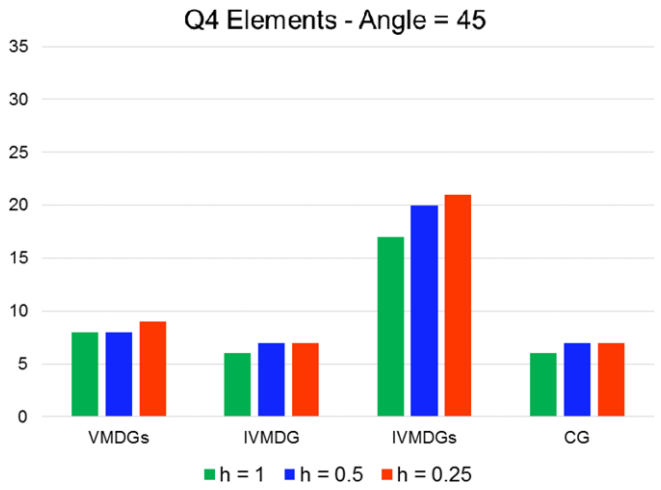

Fig. 21. Number of Newton–Raphson iterations for levels of mesh refinement, linear quadrilaterals, $E_f/E_m = 1.0$, $\theta = 45°$.

As a representative result, the number of iterations required for each method as mesh refinement is applied is shown in Fig. 21. In particular, this case corresponds to meshes of linear quadrilateral elements with $E_f = E_m$ and $\theta = 45°$. Each of the CG, IVMDG, and VMDGs methods demonstrate uniform performance with respect to the mesh resolution. The IVMDGs method is more sensitive, consistent with the behavior found in Fig. 20.

Overall, the trends observed in this section were analogous to those from Sections 4.2 and 4.3, particularly nonlinear iterative performance in Figs. 11 and 20. Therefore, we conclude that the conclusions drawn in the case of material isotropy may also be extended to problems exhibiting anisotropic material response.

5. Conclusion

We have proposed and systematically analyzed a series of algorithmic modifications to a finite strain stabilized Discontinuous Galerkin (DG) method [1], herein denoted as VMDG. The major aim of the modifications is to improve the cost effectiveness of the original method as well as simplify its implementation while retaining its robustness and stability. Namely, specific terms in the nonlinear and incremental weak forms are selectively neglected, resulting in a family of methods summarized in Table 1 of Section 3. Each of these modifications has important effects on the mathematical and algorithmic properties of the DG method, including accuracy and stability as well as variational, adjoint, and algorithmic consistency. For example, while the VMDG method possesses a symmetric consistent tangent matrix, certain proposed modifications yield non-symmetric tangent stiffness matrices.

To analyze these properties of the VMDG algorithmic family, a comprehensive numerical study was conducted across a range of two and three-dimensional problems addressing h and p refinement, various hyperelastic materials, and large strains and rotations. The first three problems possessed exact analytical solutions such that the accuracy of the computed solutions could be unambiguously measured and convergence rates could be obtained in various error norms. The fourth problem involved more complex material response and served as a means to quantify the number of iterations required during the Newton–Raphson solution procedure, one of the key measures of computational cost alongside the element-level calculations. The consistent numerical performance across all element types indicates that the generality of the VMDG method is not compromised by the algorithmic modifications. Additionally, these studies highlighted the tensorial nature and nonlinear evolution of the consistently derived stability tensors $\boldsymbol{\tau}_S^{(\alpha)}$ contained within the numerical flux and other interface terms of the VMDG formulation, which is a defining feature of the method.

Our conclusion from the study is that the VMDGs method is the optimal member of the proposed algorithmic family. This method has exactly the same nonlinear weak form as the VMDG method and therefore inherits all of its underlying mathematical properties. The only modification is the dropping of the sixth-order tensor term from the incremental weak form, leading to 50% cost savings at the element level while retaining the symmetry of the stiffness matrix and only adding a relatively small number of iterations to the Newton–Raphson scheme. The other strong candidate emerging from the study is the IVMDG method, which contains the fewest number of interface terms to be evaluated and is therefore the least expensive at the element level. This method exhibits a quadratic rate of convergence during the Newton–Raphson solution procedure and produces solutions on coarse meshes with comparable accuracy to the VMDG method. However, the downsides to the IVMDG method are the lack of symmetry in the consistent tangent matrix and the possible suboptimal convergence rate in the L^2 norm of displacement error upon mesh refinement.

More generally, the results of these extensive numerical studies provide valuable insight into the performance of Discontinuous Galerkin methods in the context of finite strain hyperelasticity. In particular, the weak forms of various members of the VMDG family share features with other existing DG methods [3–5,8], where the distinguishing feature herein is the enhanced definition of the numerical flux and stability parameters at the interface. By way of this similarity, the present results and conclusions complement these preceding works and empower the end-user to select the optimal method accounting for their computing architecture and desired numerical performance.

Acknowledgment

P. Chen was partially supported by a research grant FA8650-13-C-5214 from US-AFRL. This support is gratefully acknowledged.

References

[1] T.J. Truster, P. Chen, A. Masud, Finite strain primal interface formulation with consistently evolving stabilization, Internat. J. Numer. Methods Engrg. 102 (2015) 278–315.
[2] D.N. Arnold, F. Brezzi, B. Cockburn, L.D. Marini, Unified analysis of discontinuous Galerkin methods for elliptic problems, SIAM J. Numer. Anal. 39 (2002) 1749–1779.
[3] L. Noels, R. Radovitzky, A general discontinuous Galerkin method for finite hyperelasticity. Formulation and numerical applications, Internat. J. Numer. Methods Engrg. 68 (2006) 64–97.
[4] R. Liu, M.F. Wheeler, I. Yotov, On the spatial formulation of discontinuous Galerkin methods for finite elastoplasticity, Comput. Methods Appl. Mech. Engrg. 253 (2013) 219–236.
[5] V.D. Nguyen, G. Becker, L. Noels, Multiscale computational homogenization methods with a gradient enhanced scheme based on the discontinuous Galerkin formulation, Comput. Methods Appl. Mech. Engrg. 260 (2013) 63–77.
[6] M.G. Larson, A.J. Niklasson, Analysis of a family of discontinuous Galerkin methods for elliptic problems: the one dimensional case, Numer. Math. 99 (2004).
[7] R. Hartmann, Adjoint consistency analysis of discontinuous Galerkin discretizations, SIAM J. Numer. Anal. 45 (2007) 2671–2696.
[8] J. Mergheim, P. Steinmann, A geometrically nonlinear FE approach for the simulation of strong and weak discontinuities, Comput. Methods Appl. Mech. Engrg. 195 (2006) 5037–5052.
[9] A. Ten Eyck, A. Lew, Discontinuous Galerkin methods for non-linear elasticity, Internat. J. Numer. Methods Engrg. 67 (2006) 1204–1243.

[10] A.T. Eyck, F. Celiker, A. Lew, Adaptive stabilization of discontinuous Galerkin methods for nonlinear elasticity: Motivation, formulation, and numerical examples, Comput. Methods Appl. Mech. Engrg. 197 (2008) 3605–3622.
[11] F. Brezzi, T.J.R. Hughes, L.D. Marini, A. Masud, Mixed discontinuous Galerkin methods for Darcy flow, J. Sci. Comput. 22 (2005) 119–145.
[12] B. Cockburn, J. Gopalakrishnan, R. Lazarov, Unified hybridization of discontinuous Galerkin, mixed, and continuous Galerkin methods for second order elliptic problems, SIAM J. Numer. Anal. 47 (2009) 1319–1365.
[13] C.O. Faria, A.F.D. Loula, A.J.B. dos Santos, Primal stabilized hybrid and DG finite element methods for the linear elasticity problem, Comput. Math. Appl. 68 (2014) 486–507.
[14] N.C. Nguyen, J. Peraire, Hybridizable discontinuous Galerkin methods for partial differential equations in continuum mechanics, J. Comput. Phys. 231 (2012) 5955–5988.
[15] H. Kabaria, A.J. Lew, B. Cockburn, A hybridizable discontinuous Galerkin formulation for non-linear elasticity, Comput. Methods Appl. Mech. Engrg. 283 (2015) 303–329.
[16] T.J.R. Hughes, Multiscale phenomena: Green's functions, the Dirichlet-to-Neumann formulation, subgrid scale models, bubbles and the origins of stabilized methods, Comput. Methods Appl. Mech. Engrg. 127 (1995) 387–401.
[17] T.J. Truster, A. Masud, Primal interface formulation for coupling multiple PDEs: A consistent derivation via the variational multiscale method, Comput. Methods Appl. Mech. Engrg. 268 (2014) 194–224.
[18] A. Masud, T.J. Truster, L.A. Bergman, A unified formulation for interface coupling and frictional contact modeling with embedded error estimation, Internat. J. Numer. Methods Engrg. 92 (2012) 141–177.
[19] C. Annavarapu, M. Hautefeuille, J.E. Dolbow, A robust Nitsches formulation for interface problems, Comput. Methods Appl. Mech. Engrg. 225 (2012) 44–54.
[20] A. Masud, T.J. Truster, A framework for residual-based stabilization of incompressible finite elasticity: Stabilized formulations and $\bar{F}$ methods for linear triangles and tetrahedra, Comput. Methods Appl. Mech. Engrg. 267 (2013) 359–399.
[21] R. Liu, M.F. Wheeler, C.N. Dawson, A three-dimensional nodal-based implementation of a family of discontinuous Galerkin methods for elasticity problems, Comput. Struct. 87 (2009) 141–150.
[22] P.D. Lax, A.N. Milgram, Parabolic equations, in: Contributions to the Theory of Partial Differential Equations, Princeton University Press, Princeton, NJ, 1954, pp. 167–190.
[23] T. Oliver, D. Darmofal, Analysis of dual consistency for discontinuous Galerkin discretizations of source terms, SIAM J. Numer. Anal. 47 (2009) 3507–3525.
[24] R. Becker, R. Rannacher, An optimal control approach to a posteriori error estimation in finite element methods, Acta Numer. 10 (2001) 1–102.
[25] B.A. de Dios, F. Brezzi, O. Havle, L.D. Marini, L2-estimates for the DG IIPG-0 scheme, Numer. Methods Partial Differential Equations 28 (2012) 1440–1465.
[26] A. Masud, R. Calderer, A variational multiscale stabilized formulation for the incompressible Navier–Stokes equations, Comput. Mech. 44 (2009) 145–160.
[27] J.C. Simo, R.L. Taylor, Consistent tangent operators for rate-independent elastoplasticity, Comput. Methods Appl. Mech. Engrg. 48 (1985) 101–118.
[28] C. Miehe, Numerical computation of algorithmic (consistent) tangent moduli in large-strain computational inelasticity, Comput. Methods Appl. Mech. Engrg. 134 (1996) 223–240.
[29] C. Dawson, S. Sun, M.F. Wheeler, Compatible algorithms for coupled flow and transport, Comput. Methods Appl. Mech. Engrg. 193 (2004) 2565–2580.
[30] J. Sanders, M.A. Puso, An embedded mesh method for treating overlapping finite element meshes, Internat. J. Numer. Methods Engrg. 91 (2012) 289–305.
[31] R. Liu, M.F. Wheeler, C.N. Dawson, R.H. Dean, A fast convergent rate preserving discontinuous Galerkin framework for rate-independent plasticity problems, Comput. Methods Appl. Mech. Engrg. 199 (2010) 3213–3226.
[32] B. Rivière, M.F. Wheeler, V. Girault, Improved energy estimates for interior penalty, constrained and discontinuous Galerkin methods for elliptic problems. Part I, Comput. Geosci. 3 (1999) 337–360.
[33] J.E. Dolbow, L.P. Franca, Residual-free bubbles for embedded Dirichlet problems, Comput. Methods Appl. Mech. Engrg. 197 (2008) 3751–3759.
[34] T.J. Truster, A. Masud, A discontinuous/continuous Galerkin method for modeling of interphase damage in fibrous composite systems, Comput. Mech. 52 (2013) 499–514.